Construction and Building Materials 320 (2022) 126297

Contents lists available at ScienceDirect

Construction and Building Materials

journal homepage: www.elsevier.com/locate/conbuildmat

Multi-objective optimisation design for GFRP tendon reinforced cemented soil

Genbao Zhang [a,c], Changfu Chen [d,e], Kefei Li [f], Fan Xiao [g], Junbo Sun [b,*], Yufei Wang [h,*], Xiangyu Wang [h]

[a] College of Civil Engineering, Hunan City University, Yiyang, Hunan 413000, PR China
[b] Institute for Smart City of Chongqing University in Liyang, Chongqing University, Jiangsu, 213300, PR China
[c] Hunan Engineering Research Center of Structural Safety and Disaster Prevention for Urban Underground Infrastructure, Yiyang, Hunan 413000, PR China
[d] Key Laboratory of Building Safety and Energy Efficiency of the Ministry of Education, Hunan University, Changsha, Hunan 410082, PR China
[e] College of Civil Engineering, Hunan University, Changsha, Hunan 410082, PR China
[f] School of Civil and Environmental Engineering, University of New South Wales, Sydney, NSW 2052, Australia
[g] College of Management, Zhongkai University of Agriculture and Engineering, Guangzhou, 510225, PR China
[h] School of Design and Built Environment, Curtin University, Perth, WA 6102, Australia

ARTICLE INFO

Keywords:
Cemented soil
Element pullout test
Interface bond strength
Unconfined compressive strength
Glass fiber reinforced polymer reinforcement
Machine learning
Multi-objective optimisation

ABSTRACT

Rebar reinforced cemented soil is employed widely to solve the weak foundation problem led by sludge particularly. Nowadays, the glass fiber-reinforced polymer (GFRP) becomes a new tendon material instead of steel to avoid the performance degradation resulting from steel corrosion. The interface bond strength of GFRP tendon-reinforced cemented soils (GTRCS) displays its excellent mechanical capacity. Nevertheless, its application is obstructed by the deficient studies between the bond strength and influence factors. Therefore, this study investigates the effects of varying water contents (C_w: 50%-90%), cement proportions (C_c: 6%-30%), and curing periods (T_c: 28 days, 90 days) on both pullout strength (T_p) and unconfined compression strength (UCS) of GTRCS. The results showed that the pullout strength and compressive strength were positively related to T_c and C_c and negatively related to C_w. Besides, these experimental results were also utilised to develop support vector regression (SVR) models. The beetle antennae search (BAS) algorithm was used to adjust the SVR's hyperparameters. The high correlation coefficients (0.988 for UCS and 0.972 for T_p) proved the reliability of the established BAS-SVR models. In addition, the multi-objective beetle antennae search algorithm (MOBAS-SVR) was developed for bi-objective optimisation designs (UCS-cost and T_p-cost). Finally, sensitivity analysis was conducted to range the significance of variables for T_p and UCS.

1. Introduction

Cement is extensively applied in foundation improvement and stabilisation to avoid sludge-induced problems particularly [1-3]. Cement-soil composite is generated from the pozzolanic activities caused by cement filling the pores in sludge using soil mixing technique. The characteristics of this mixed material are enhanced compared to that of the soil [4,5]. Even so, only cement-soil composite alone is deficient to withstand the lateral earth pressure in foundation pit support and blocking surface water. The utilization of steel rebar as part of the structure combined with cement-soil matrix is one safer way to sustain the exterior load [6-9]. However, the performance of the whole composite is inevitably degraded by the steel corrosion during its usage which has an especially serious impact on permanent structures [10-13]. In case of degradation, the glass fiber-reinforced polymer (GFRP) becomes a new tendon material to displace the steel for its excellent engineering characteristics and high affordability [14].

The interface bond performance of GFRP tendon-reinforced cemented soils (GTRCS) presents their pullout capability, in analogy to reinforced concrete [15-17]. In many circumstances, failures are induced by the bonding surface detachment but not the tendon reaching its ultimate strength. Although it is essential, the interface-bond-strength-related

* Corresponding authors.
E-mail addresses: genbao@hncu.edu.cn (G. Zhang), cfchen@hnu.edu.cn (C. Chen), kefei0415@163.com (K. Li), chiufan1025@outlook.com (F. Xiao), tunneltc@gmail.com (J. Sun), wangyf0113_suz@163.com (Y. Wang), Xiangyu.Wang@curtin.edu.au (X. Wang).

https://doi.org/10.1016/j.conbuildmat.2021.126297
Received 7 September 2021; Received in revised form 20 December 2021; Accepted 30 December 2021

failure patterns are still indeterminate resulting in insufficient design codes of reinforced cement-soil structures [6,18]. Furthermore, preceding studies are mainly about cemented soil's mechanical and hydraulic capacities with few concerning the bond performance between soil and GFRP reinforcements [19,20]. These obstruct the application of GTRCS in practice. Therefore, the investigation related to the interface bonding strength of GTRCS is necessary. This research can also be used for future application to compare with concrete structures [21-25].

To this end, some influencing factors are explored for the bonding strength of GTRCS. Cement-soil composite consists of cement, soil, and water with its mechanical properties being affected by them [26]. Moreover, the relative slip displacement (S_p) between cemented soil and tendons is another factor to influence the interface bond strength of GTRCS [27,28]. Since the structure and texture of cemented soil similar to that of concrete instead of soil, the dry density and degree of saturation (conventional parameters for soil) is not considered as the parameter in this study. Thereby, water content (C_w), cement content (C_c), curing time (T_c), and S_p are four variables in this study. The test process is laborious because of complicated facilities and numerous samples. Moreover, the subsequent result analysis is hindered because the traditional data analysing methodologies have defects in error control and obtaining the optimal mix proportion under multivariable conditions [29-31]. These methods based on linear or nonlinear regression equations also have difficulties in the actual application because of the experience requirements for selecting equations and generalisation of handling variables [32,33]. Hence, machine learning (ML) models such as artificial neural network (ANN) and random forest (RF) [34-36] were proposed to process complex nonlinear problems and obtain accurate results. Support vector regression (SVR) is another one of the most widely used ML models in the data processing field [37,38]. Researchers well accepted SVR because of its outstanding generalisation capability and quick computation operation compared to other ML models [39]. Besides, it enables to deal with classification and regression problems, including linear or nonlinear issues [40,41]. The regression functions developed by SVR could map into higher dimensional spaces to eliminate the complexity of the computation process [42,43]. Accordingly, this ML model was adopted in this study for data analysis.

Although with excellence in utilization, SVR performance depends heavily on its hyperparameters, which encounter difficulties adjusting through conventional optimisation means [44]. The grid search method is one of the most commonly used conventional optimisation methods to search the optimal hyperparameters of SVR. However, the computation complexity is very high, which is mainly because of the searching mechanism that the exhaustive parameter combinations are tested through cross validation [45]. To solve this, several optimisation algorithms were introduced, like the genetic algorithm (GA), firefly algorithm (FA), and particle swarm optimisation (PSO) [46-48]. However, these algorithms require high demand in computation compared to the beetle antennae search (BAS) algorithm, which converges and calculates quickly [49-51]. Besides, Huang, et al. (2007) developed the method of uniform design to automatically search the hyperparameters of support vector machine [52]. In this study, the BAS algorithm was selected to tune hyperparameters of SVR in the processing progress (BAS-SVR).

For cement-soil optimal design of this study, mechanical performances, including pullout strength (T_p) and unconfined compressive strength (UCS), were required to achieve a balance with cost. Therefore, the BAS-SVR based multi-objective optimisation model (MOBAS-SVR) was developed through a metaheuristic algorithm to address this problem. By introducing Pareto solutions, the multi-objective optimisation (MOO) can achieve the maximum efficiencies of two or more objectives. For instance, Naseri et al. (2019) utilised particle swarm optimisation and genetic algorithm to achieve the optimal goal of no-slump concrete [53]. Therefore, it is necessary to propose a MOO model maximizing utilization of the objectives within experiments.

This study researched a sum of 150 groups of cement-soil specimens for laboratory experiments, obtaining corresponding 150 pullout strengths (T_p) and mean UCS. Depending on the overall laboratory data, highly accurate SVR models were established with the hyperparameters tuned by the BAS algorithm. Afterward, the bi-objective optimisation design, including T_p-cost and UCS-cost, were fulfilled by the MOBAS-SVR model by proposing the Pareto solutions. At last, the influence of input variables (C_c, C_w, T_c, S_p) was ranked based on a sensitivity analysis.

2. Experimental programs

2.1. Materials

The soil was gathered from the floodplain at the confluence of Xiangjiang and Jinjiang River in Changsha, China. It was air-dried, ground in a machine, and then sifted out. Only particles with a diameter less than 5 mm were reserved to gain uniform granularity and the particle-size distribution is presented in Fig. 1. The ordinary Portland cement with a strength grade of 42.5 and GFRP tendons with 230 mm in height were selected to form GTRCS as pullout specimens. The properties of the soil sample, cement, and GFRP tendons are presented in Table 1.

2.2. Mixture design

C_w, C_c, and T_c are the three main influence variables of GTRCS performance as mentioned before. Water and cement contents are defined as below:

$$C_w = \frac{m_w}{m_s} \tag{1}$$

$$C_c = \frac{m_c}{m_w + m_s} \tag{2}$$

where m_w means the weight of the water added; m_s is the weight of the dry soil; m_c denotes the weight of the cement.

C_w ranged from 50% to 90% in this study because areas where cemented stabilization is widely applied usually feature clay with water content near the liquid limit. C_c was designed between 6% and 30% to offer sufficient workability and optimum stabilization efficiency [54]. Besides, composites cured for 15 to 30 days are widely used in practice to solve problems such as tight schedules [54]. In ground improvement applications, the hydration and hardening process for the cemented soil acquires at least 90 days to develop the full strength [55]. Hence, 5 stepwise increasing levels were chosen for C_w and C_c, and 6 levels for T_c with specific details shown in Table 2. In total, 150 GTRCS specimens were prepared in this study (5 levels for C_c × 5 levels for C_w × 6 levels for T_c).

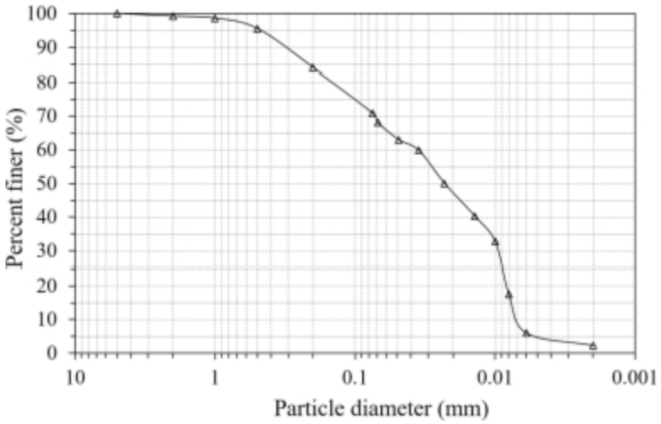

Fig. 1. Detailed particle sizes of soil sample.

Table 1
Materials used in the experimental program.

Properties	Values
Soil	
Specific gravity	2.705
Natural moisture content (%)	30–90
Liquid limit (%)	58.1
Plasticity limit (%)	28.6
Cement	
Type	P.O 42.5
Specific gravity (t/m^3)	3.0–3.2
Compressive strength (MPa)	≥42.5 (28-day)
Normal consistency (%)	27
GFRP reinforcement	
Type	GFRP tendon
Rib spacing (mm)	10.1
Tensile strength (MPa)	466
External diameter (mm)	16.8
Internal diameter (mm)	15
Young's modulus (GPa)	40

Table 2
Influence variables with all levels used in the experimental project.

Influence factor	Number of levels	Magnitude
Water content C_w (%)	5	50, 60, 70, 80, 90
Cement content C_c (%)	5	6, 12, 18, 24, 30
Curing duration T_c (days)	6	7, 14, 28, 42, 60, 90

2.3. Pullout test

To prepare cement-soil composites for pullout test, soil and cement samples were mixed for a first 60-second and another 480-second with water added. The GFRP tendon was installed in the middle of the pullout cell, as presented in Fig. 2. The cell's internal surface was lubricated to lower the boundary friction and its bottom was sealed with paper plates to avoid leaking. After that, the cemented soil was placed into the pullout cell which was then vibrated to make the density even. Fig. 3 depicts the images of GFRP tendon and cemented soil that placed in the cell. Subsequently, each cell was sealed with a plastic bag and cured for a predetermined time. The paper plates were removed in case of extra adhesion after 7-day curing.

After curing the sample at specific ages, the pullout test is conducted using a pile interface friction testing system (PIFTS) presented in Fig. 4. The tendon's top was fixed to the load cell and the GTRCS sample was installed on the mobile platform which conducted the pullout force on the tendon. The platform and a constraining plate held the specimen tightly to guarantee proper interface shear displacement while it was descending 1.0 mm/min. The load cell and linear variable differential transformer (LVDT) recorded the load and corresponding displacement. The cemented soil and tendon were completely detached as soon as the platform got a 20-mm displacement, and operators ended the loading process [10,56]. Eventually, 15 pullout strengths at corresponding interface slip distances were obtained for each specimen, shown in Appendix.

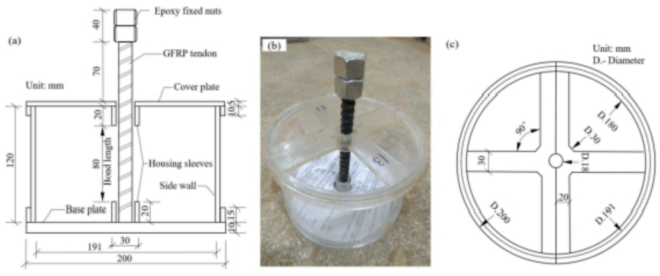

Fig. 2. Details of pullout cell: (a) diagram of cross-sectional elevation, (b) three-dimension view of cell, and (c) diagram of cross-sectional plan.

2.4. Unconfined compression test

The procedure of sample preparation for the unconfined compression test is the same as that prepared for the pullout test. These samples were initially prepared in cubic forms with the dimensions of 10 cm and then conducted by the TYA-2000S Electron-Hydraulic compression machine with 0.01 KN precision. The loading rate was 0.03–0.15 KN/S during the process, and failures happened when compressive forces exceeded the capacities of specimens. The corresponding stress was used as the samples' compressive strength, calculated from the ratio between failing force and their cross-section area.

3. Multi-objective optimisation approach

The schematic illustrations of the whole process for MOBAS-SVR operation to obtain optimal GTRCS mixtures were shown in Fig. 5. The initial procedure was proposals of two SVR models to predict UCS and T_p. To obtain desired models, their involving hyperparameters were adjusted through the BAS algorithm based on 10-fold cross-validations (CV). Then, the expense was determined for each mix. The weighted sum method was utilised for building up a multi-target work and the Pareto front was created to show the enhancement blend plan of GTRCS. The ML and optimisation experiments were both implemented through Matlab R2020a.

3.1. Data description

As mentioned before, the variables are the cement content, water content, curing ages, and slip displacement. These variables can be used to calculate the amounts of the raw materials (cement, water, and soil). The outputs are the compressive strength and pullout strength with their datasets derived from the mechanical tests. The raw material information and output factors are summarised in Table 3 for UCS and Table 4 for T_p.

The relationships between input variables are visualized using a correlation matrix in Fig. 6, representing the Pearson correlation coefficients between any two different variables. Pearson correlation coefficient is a commonly used method to evaluate the degree of correlation between variable X and variable Y. On condition that the coefficients are not larger than 0.5, the correlation between these input variables are supposed to be small. In this case, the multi-collinearity problems will not be produced reducing the prediction error. It can be observed that only the coefficient between cement and water is around 0.5 and others are close to zero. This is reasonable since only the cement and water are designed based on the C_c (6% to 30%) and C_w (50% to 90%) while the other variables are independent such as curing time, slip displacement, and soil. In this manner, the fundamental BAS-SVR model of the optimal multi-objective scheme was proposed.

3.2. Establishment of BAS-SVR model

3.2.1. Support vector regression (SVR)

SVR is a popular regression model proposed by Vapnik (1995). It uses a kernel function to project original data from its space to high-dimensional space, and then solve nonlinear problems. The data is described as (x_i, y_i) where x_i and y_i are the one-dimensional vector and scalar regression value, respectively. For its groups, the training dataset has the limit value of n like (x_n, y_n). The regression function is expressed in the linear equation form as Equation (3) where w, β, and $\varphi(x)$ are the weight vector, bias, and a mapping function.

$$f(x) = w \bullet \varphi(x) + \beta \tag{3}$$

The loss function is described as Equation (4) used to calculate the deviation extent from the predicted to actual values (e is the largest

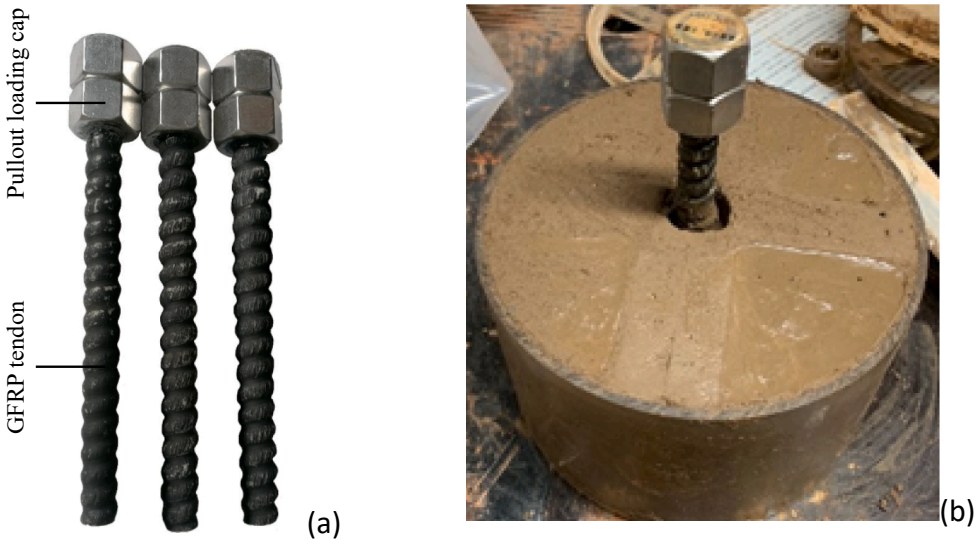

Fig. 3. The images of GFRP tendon and cemented soil in the cell.

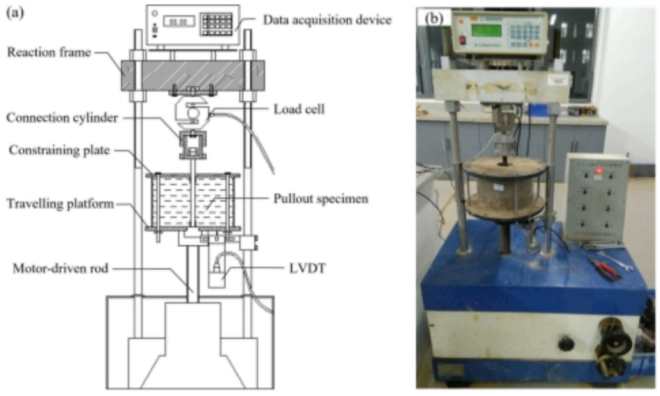

Fig. 4. The (a) schematic diagram and (b) actual application of PIFTS.

tolerance error).

$$\mathscr{L}(x,y,f) = |y_i - f(x_i)|_e = \begin{cases} 0, |y_i - f(x_i)| < e \\ |y_i - f(x_i)| - e_i, |y_i - f(x_i)| \geq e \end{cases} \quad (4)$$

Considering the minimum structural risk, the problem is described as follows.

$$\mathscr{R}(w) = \frac{1}{2}\|w\|^2 + \sum_{i=1}^{n} \mathscr{L}(x,y,f) \quad (5)$$

the slack variables δ_i and δ_i^* are utilised to improve the tolerance of biased data. Equation (5) can be converted to a convex optimise function in the following manner.

$$min_{w,e,\delta,\delta^*} \mathscr{R}(w) = \frac{1}{2}\|w\|^2 + C\sum_{i=1}^{n}\left(\delta_i + \delta_i^*\right)$$

Table 3
Detailed information of input and output variables in the UCS aspect.

Variables	Minimum	Maximum	Mean	Std Dev
Cement (kg/m^3)	87	438	259	113
Water (kg/m^3)	487	684	594	52
Soil (kg/m^3)	681	1102	848	118
Curing age (day)	7	90	35	28
UCS (kPa)	31	10,255	1274	2214

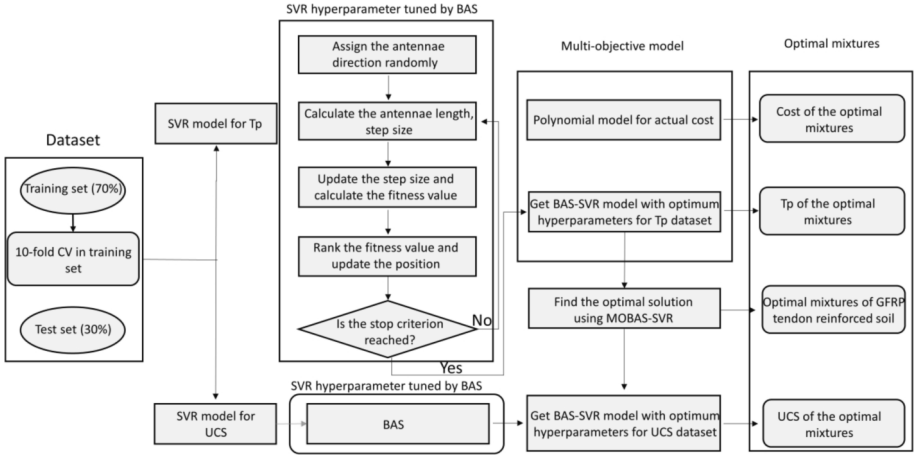

Fig. 5. Schematic descriptions of the MOBAS-SVR system to obtain optimal GTRCS mixtures.

Table 4
Detailed information of input and output variables in the UCS aspect.

Variables	Minimum	Maximum	Mean	Std Dev
Cement (kg/m^3)	87	438	259	113
Water (kg/m^3)	487	684	594	52
Soil (kg/m^3)	681	1102	848	118
Curing age (day)	7	90	28	28
Slip displacement (mm)	1	20	5	6
T_p (kPa)	0	5332	216	774

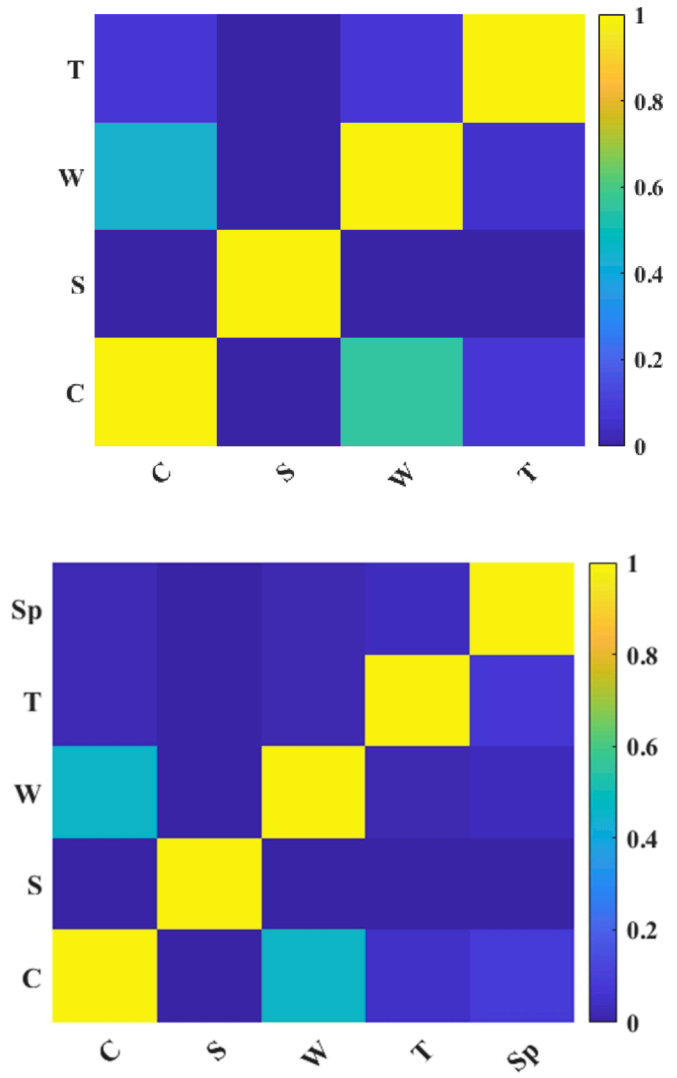

Fig. 6. Correlation diagrams of influencing factors in mechanical performances (a) the UCS (b) the.T_p

$$s.t\begin{cases} y_i - w\cdot\varphi(x) - \beta \le e + \delta_i \\ w\cdot\varphi(x) + \beta - y_i \le e + \delta_i^* \\ \delta_i \ge 0 \\ \delta_i^* \ge 0 \end{cases} \tag{6}$$

where C represents the penalty coefficient calculated with respect to a few differences between regression lines and samples out of the e-tube. The schematic figure of SVR is shown in Fig. 7. By introducting positive Lagrange multipliers (a_i, a_i^*, u_i, u_i^*), a dual-issue can be obtained as Equation (7).

$$L(w,\beta,\delta,a,u) = \frac{1}{2}\|w\|^2 + C\sum_{i=1}^{n}(\delta_i + \delta_i^*)$$
$$- \sum_{i=1}^{n} a_i(e + \delta_i - y_i + w\cdot\varphi(x_i) + \beta)$$
$$- \sum_{i=1}^{n} a_i^*(e + \delta_i + y_i - w\cdot\varphi(x_i) - \beta)$$
$$- \sum_{i=1}^{n}(u_i\delta_i + u_i^*\delta_i^*) \tag{7}$$

When an imperative condition is fully inversely opposite and the target equation is different, all of the first and both points of Equation (8) should be completed by the Kush-Kuhn-Tuck (KKT) Rules [58]. According to this rule, the results of dual variables and corresponding constraints are 0 in Equation (9). Besides, the weight factor w is in the form of $\sum_{i=1}^{n}(a_i - a_i^*)\varphi(\boldsymbol{x}_i)$.

$$\begin{cases} \dfrac{\partial L}{\partial w} = w - \sum_{i=1}^{n}(a_i - a_i^*)\varphi(x_i) = 0 \\ \dfrac{\partial L}{\partial \beta} = \sum_{i=1}^{n}(a_i - a_i^*) = 0 \\ C - a_i - u_i = 0 \\ C - a_i^* - u_i^* = 0 \end{cases} \tag{8}$$

$$\begin{aligned} a_i(e + \delta_i - y_i + w\cdot\varphi(x_i) + \beta) = 0 \\ a_i^*(e + \delta_i + y_i - w\cdot\varphi(x_i) - \beta) = 0 \\ (C - a_i)\delta_i = 0 \\ (C - a_i^*)\delta_i^* = 0 \end{aligned} \tag{9}$$

After solving the above equations, the language dual problem is derived as follows:

$$max_i\left(-\frac{1}{2}\sum_{i=1}^{n}\sum_{j=1}^{n}(a_i - a_i^*)\left(a_j - a_j^*\right)x_j^T x_j - e\sum_{i=1}^{n}(a_i - a_i^*) + \sum_{i=1}^{n} y_i(a_i - a_i^*)\right)$$

$$s.t\begin{cases} \sum_{i=1}^{n}(a_i - a_i^*) = 0 \\ a_i, a_i^* \in [0, C] \end{cases} \tag{10}$$

And the final regression function is shown as Equation (11).

$$f(x) = \sum_{i=1}^{n}(a_i - a_i^*)\varphi(x_i)x + \beta \tag{11}$$

3.2.2. Beetle antennae search (BAS)

BAS is a metaheuristic algorithm to spontaneously search the most desirable hyperparameters of ML models, deriving from the longhorn beetle behaviour simulation [59]. The beetle uses its two antennae to detect smell concentration and moves towards the direction where the concentration is strongest. The positions of the left and right antennae are represented as the symbols x_l^i and x_r^i with superscript i illustrating the i^{th} time instant. As a result, Equation (12) can be used to calculate the location of antennae instantly.

$$x_l^i = x^i + d^i b$$
$$x_r^i = x^i - d^i b \tag{12}$$

where b is a random vector illustrating the beetle's randomized movement. The vector can be represented as Equation (13) by introducing the

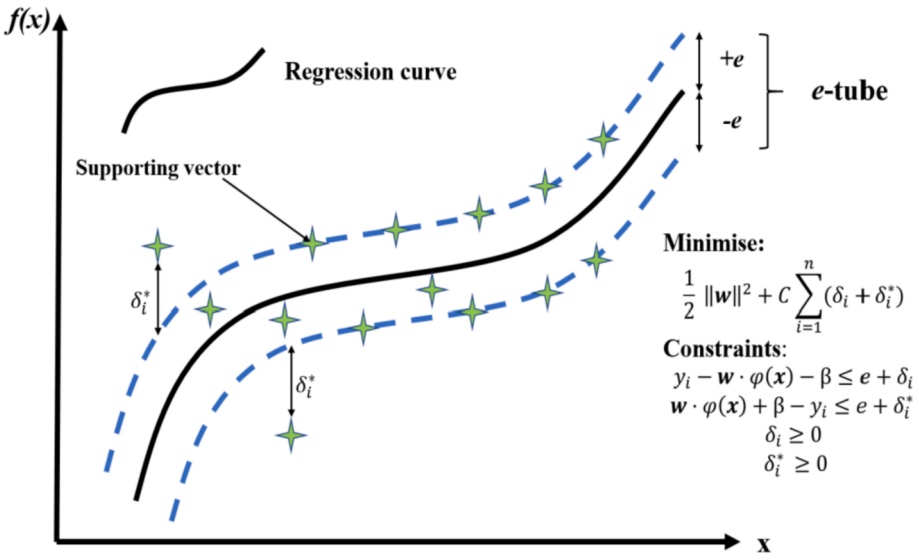

Fig. 7. A support vector regression machine [57]

rand and *k*, which represent a random function and the dimension, respectively.

$$b = \frac{rand(k,1)}{\|rand(k,1)\|} \tag{13}$$

The vector indicating beetle position is shown in the following equations, where δ denotes the step distance and $f(x)$ means the fitness function. In addition, the length of the antennae and the step distance may be changed through the following BAS pseudocode, illustrated in Fig. 8.

$$x^i = x^{i-1} + \delta^i bsign\left(f\left(x_r^i\right) - f\left(x_l^i\right)\right) \tag{14}$$

$$d^i = 0.95d^{i-1} + 0.01 \tag{15}$$

$$\delta^i = 0.95\delta^{i-1} \tag{16}$$

3.3. Cross fold validation

The overfitting issue caused by limited numbers of data is a difficult problem that may be resolved by 10-fold cross-validation (CV) shown in Fig. 9. All the data is used for ML through CV, giving a fair and comprehensive evaluation metric when the database is small. Particularly, the hyperparameters are adjusted on a randomly segmented training set (the external training set) that accounts for seventy percent of the samples [45]. Afterward, the external training set is divided into two parts: a validation set (ten percent of the training set) and an internal training set (ninety percent of the training set). Since the validation set is mainly used to compare the performance of established models within cross validation, ten percent of the training set is supposed to be appropriate. On the internal training set, the model is established with BAS searching for the optimal hyperparameters. After training process, the validation set's root-mean-square error (RMSE) is subsequently obtained to evaluate the model's properties. This procedure is repeated ten times corresponding to 10-fold cross validation. Finally, the ML model trained by the training set with prime hyperparameters (chosen from the minimum RMSE values) is evaluated for the test set (30% of dataset).

In this research, the root mean square error (RMSE), correlation coefficient (*R*), mean absolute percentage error (MAPE), and mean

Input fitness function $f(x)$, initial step size δ^0 and position of beetle x^0, maximum iterations t, and the ratio of antennae length to step distance c
Output the most desirable position x_b, as well as fitness function figure $f(b)$
For $i = 1$ *to* n
  Generate random antennae direction b
  Calculate the antennae length $d^i = c \times \delta^i$, the positions x_l^i and x_r^i, and the fitness function value $f(x_l^i)$ and $f\left(x_r^i\right)$ at the wing antennae positions
  Calculate the next location x_l^{i+1} and the fitness function figure $f(x^{i+1})$
  If $f\left(x^{i+1}\right) < f(b)$
    Update x_b to x^{i+1}
    Update f_b to $f\left(x^{i+1}\right)$
  End
  Update step distance δ^{i+1}
End

Fig. 8. The pseudocode for BAS.

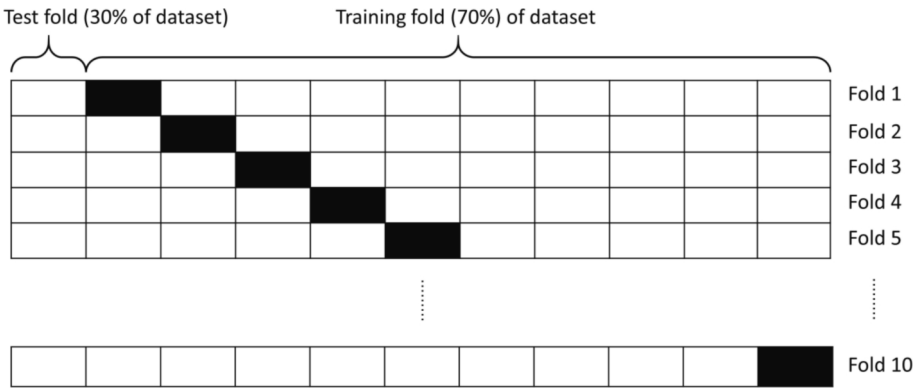

Fig. 9. 10-fold cross validation.

absolute error (MAE) employed to assess the ML models' characteristics are defined as:

$$RMSE = \sqrt{\frac{1}{N}\sum_{i=1}^{N}\left(y_i^* - y_i\right)^2} \tag{17}$$

$$R = \frac{\Sigma_{i-1}^{N}\left(y_i^* - \overline{y^*}\right)(y_i - \overline{y})}{\sqrt{\Sigma_{i=1}^{N}(y_i^* - \overline{y^*})^2}\sqrt{\Sigma_{i=1}^{N}(y_i - \overline{y})^2}} \tag{18}$$

$$MAPE = \frac{1}{N}\sum_{i=1}^{n}\left|\frac{y_i^* - y_i}{y_i}\right| \tag{19}$$

$$MAE = \frac{1}{N}\sum_{i=1}^{n}\left|y_i^* - y_i\right| \tag{20}$$

where the number of samples in the dataset is denoted by N; the predicted output of ML models is denoted by y_i^*; the real output in the dataset is denoted by y_i; the projected mean value is $\overline{y^*}$, whereas the true mean value in the dataset is $\overline{y}$.

3.4. Multi-objective optimisation

3.4.1. Objective function establishment

The established BAS-SVR model is the representing function of UCS and T_p. Meanwhile, the polynomial fuction is used as the objective function for cost as follows:

$$Cost\left(\$/m^3\right) = C_cQ_c + C_wQ_w + C_sQ_s \tag{21}$$

In Equation (21), Q_w, Q_s, Q_c represents the amount (kg/m^3) of water, soil, and cement, respectively. As for C, it indicates the unit price (kg/m^3) of components involving in GTRCS, shown in Table 5.

3.4.2. Constraints

The following constraints need to be set for MOO problems, including material range, volume, and ratio constraints. The data scope comes from the datasets of GTRCS, determining the top and bottom limitations of raw materials. The volume constraints illustrate that the amount of the cemented soil should control within unit cubic meter like Equation (22).

Table 5
The unit cost of each variable of GTRCS.

Variables	Notation	Unit price ($/kg)	Unit weight (kg/m^3)
OPC	C_c	0.057	3100
Water	C_w	0.001	1000
Soil	C_s	0.014	2650

$$V_m = \frac{Q_c}{U_c} + \frac{Q_w}{U_w} + \frac{Q_s}{U_s} \tag{22}$$

where U_c, U_w, and U_s are unit weights of cement, water, and soil, respectively.

Besides, to search for optimal GTRCS mixture, the fixed ratios are controlled for the correlation establishment of different raw materials. Table 6 summarises these constraints.

3.4.3. MOBAS-SVR establishment

The MOBAS-SVR is introduced by combining the objective functions of UCS, T_p, and cost. The weighted sum function F is shown as follows:

$$F = \sum_{k=1}^{k} w_k f_k, \sum_{k=1}^{k} w_k = 1 \tag{23}$$

where f_k is the objective function; weights (w_k) are calculated as $\frac{p_k}{K}$; p_k is the random value (from 0 to 1) with uniform distribution. In this study, two bi-objective functions showing the relationship between UCS and cost and T_p and cost can be defined as follows:

$$F_1 = w_1 \bullet \mathrm{UCS(90days)} + \mathrm{w_2} \bullet \mathrm{cost}$$

$$F_2 = w_1 \bullet \mathrm{Tp(90days)} + \mathrm{w_2} \bullet \mathrm{cost} \tag{24}$$

$$\sum_{k=1}^{2} w_k = 1 \tag{25}$$

To optimise multi-purpose objectives, the Pareto front is recommended to provide non-dominate solutions, which follows the condition that other objectives cannot be improved without deterioration. If Z is the group of feasible solutions and $\boldsymbol{x}^* \in Z$ is one of the Pareto points, $\boldsymbol{x}^*$ can be recognised that no existence of $\boldsymbol{x} \in Z$ could satisfy:

$$f_k(\boldsymbol{x}) \le f_k(\boldsymbol{x}^*) for k = 1, 2, 3, \cdots, tand \tag{26}$$

$$f_k(\boldsymbol{x}) < f_k(\boldsymbol{x}^*) for at least one k \tag{27}$$

If $f(\boldsymbol{x}^*)$ is larger than $f(\boldsymbol{x})$ for every $\boldsymbol{x}$, Pareto optimal solution $\boldsymbol{x}^*$ will be achieved. Fig. 10 shows the Pareto front that consist of several Pareto

Table 6
The constraints of GTRCS input variables.

Variables	Expressions	Lower limit	Upper limit
OPC	C_c	87	438
Water	C_w	487	684
Soil	C_s	681	1102
Water content	C_w/C_s	0.5	0.9
Cement content	$C_c/(C_w + C_s)$	0.06	0.3

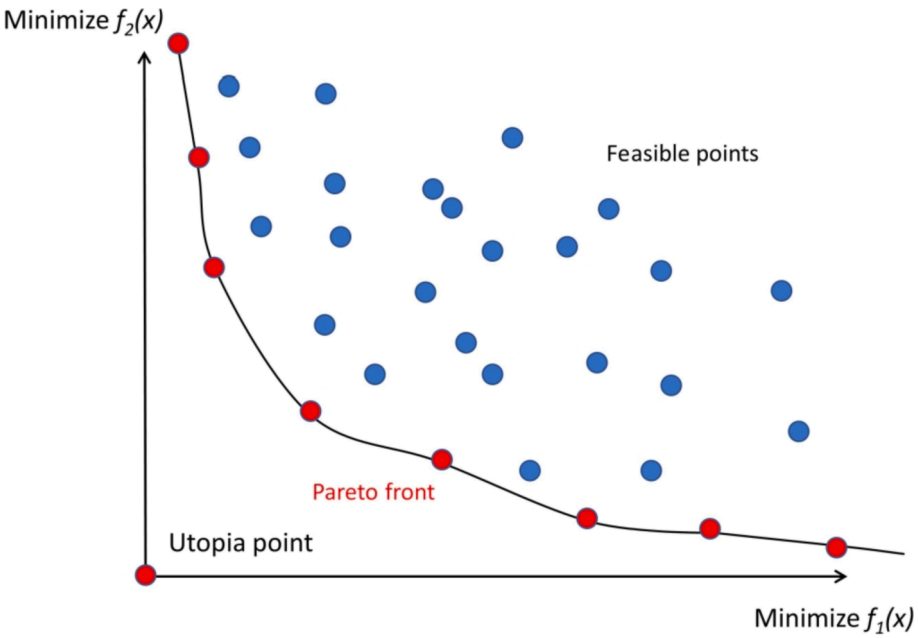

Fig. 10. Pareto front and feasible points [60]

Input: fitness function $f_1(x),\ f_2(x), \ldots, f_k(x); x = (x_1, \ldots, x_n)^T$, initial the beetle position $x^0 = (x_1^0, \ldots, x_n^0)$, initial step size $\delta^0 = (\delta_1^0, \ldots, \delta_n^0)$, maximum iterations T, antennae length/step size c, and attenuation coefficient α.
Output: M Pareto optimal positions $X_P = (X_{P,1}, \ldots, X_{P,M})$
While $m \leq M$
  Set the random weight w_k
  For i= 1 to T
    Create b^i, random antennae direction
    Measure $d^i = c \times \delta_m^i,\ x_l^i$ and x_r^i, and the weighted sum function $F(x_l^i)$ and $F(x_r^i)$
    Calculate the next position $x^{i+1} = x^i + \delta^i$ and its function value
    If $F(x^{i+1}) < F(b)$
      Update x_b to x^{i+1}, F_b to $F(x^{i+1})$
    End if
    Update δ^{i+1}
  End for
  If x_b within constraints
    If x_b is not dominated by X_P
      Update $X_P = X_P \cap x_b,\ m = m + 1$
    End if
    For $X_{P,t}$ in X_P
      If x_b dominates $x_{p,t}$
        Update $X_P = X_P - x_{p,t},\ m = m - 1$
      End if
    End for
  End if
End while

Fig. 11. The pseudocode of MOBAS.

points. In this study, the MOBAS is proposed based on BAS algorithm by the weight sum method with the pseudocode being summed up in Fig. 11.

3.4.4. Decision-making for MOO

The Pareto front, as shown before, can be used to address MOO problems, whereas the ultimate optimal mixing percentage is inadequate for decision-making. As a consequence, the Technique for Order Preference by Similarity to Ideal Solution (TOPSIS) is proposed in this study [61]. It can pick a solution that is closest to the positive ideal point (d_{i+}) and farthest from the negative ideal point (d_{i-}) simultaneously. The d_{i+} and d_{i-} are the objective function's best value and worst value, respectively. Consequently, using the following formulas, the solution with the greatest C_i is regarded as the best:

$$d_{i+} = \sqrt{\sum_{j=1}^{n}\left(F_{ij} - F_j^{ideal}\right)^2} \tag{28}$$

$$d_{i-} = \sqrt{\sum_{j=1}^{n}\left(F_{ij} - F_j^{non-ideal}\right)^2} \tag{29}$$

$$C_i = \frac{d_{i-}}{d_{i+} + d_{i-}} \tag{30}$$

where n is the total objective number and i represents the ith Pareto point; F_j^{ideal} and $F_j^{non-ideal}$ are the ideal and non-ideal values of the jth objective, respectively.

3.5. Variable importance measure

The sensitivity analysis (SA) was used to evaluate the relationship between data inputs and outputs. It can compare the influence of variables on the ML results when the input value changes. The inputs and outputs of the dataset must be pre-determined. Afterward, each variable can be analysed separately on condition that other variables remain unchanged. The SA can be used for both global and local analysis, however, locating model uncertainties cannot be achieved through local sensitivity analysis. All input variables can be assessed at the same time using global sensitivity analysis (GSA). As a consequence, GAS is used to rank the significance of numerous factors in this investigation using bar charts to demonstrate the significance of variables [62]. The following

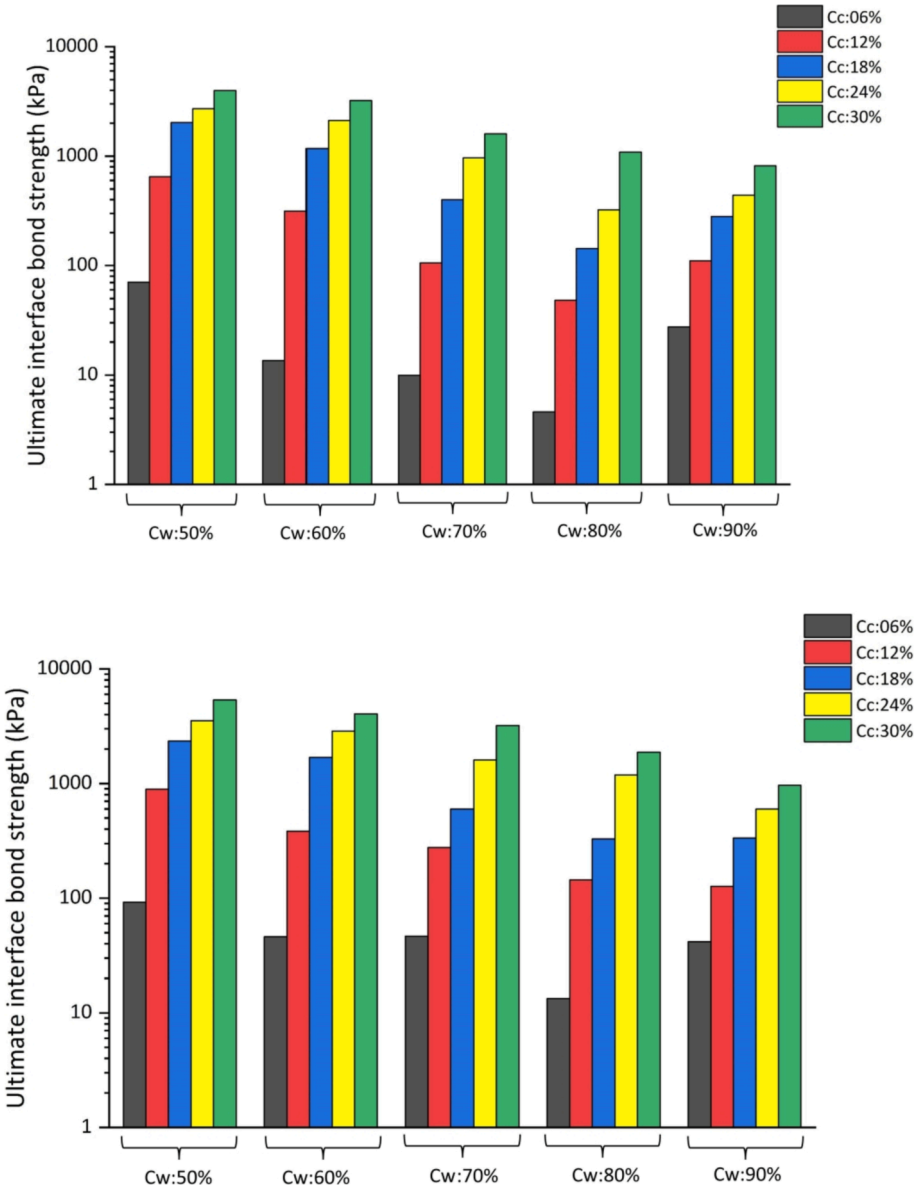

Fig. 12. The ultimate interface bond strength of samples cured at (a) 28 days (b) and 90 days.

equations provide a gradient metric for assessing output change as well as the relative significance formulation [63].

$$g_\varepsilon = \sum_{j=2}^{L} \frac{|\widehat{y_{\varepsilon,j}} - \widehat{y_{\epsilon,j-1}}|}{L-1} \tag{31}$$

$$R_\varepsilon = g_\varepsilon \Big/ \sum_{i=1}^{I} g_i \tag{32}$$

where $\widehat{y_{\varepsilon j}}$ is the sensitivity response for input $x_{\varepsilon,j}$ at j th level; R_ε is the relative importance of the variable ε; I is the number of input variables.

4. Results and discussion

4.1. Results of laboratory tests

The results of ultimate interface bond strength on the overall 150 samples are shown in Fig. 12 summarising the T_p of specimens cured at 28 days and 90 days, respectively. The increase of cement content would improve the bonding strength between cement soil and GFRP with fixed water content, which results from more cementitious products. Similar to cement, an enhanced pullout strength is achieved at a longer curing time. Conversely, the uniform 10% moisture increment in the water aspect leads to a general decreasing trend in the ultimate interface bonding performance under the same cement content. It can be attributed to the excess water developing a porous microstructure to impair the pullout strength [64-66]. However, when C_w increases from 80% to 90%, it positively influences the pullout strength, which seems to be in contrast with above findings. This is mainly because of an optimised water content (corresponding to a specific cement content), which leads to a state with the most compacted structure corresponding to the instantaneous ultimate strength. Within the range towards the optimised water content, the increasing water renders an increasing loose porous space which facilitates the growth of ettringite. The growth of strength depends essentially on the content of ettringite, which tends to expand and compact the structure of the mixture. However, within the range beyond the optimized water content, the increasing water could undermine the bond between the ettringite and the soil particles, as well as increase the pore water which weaken the bond between soil particles induced by the electrical double layer. Therefore, a strength increase when increasing water content is reasonable since the optimised water content has not been attained. In conclusion, C_c, C_w, and T_C dominates the performance of GTRCS.

Figs. 13 and 14 depict the relationship between slip distance and interface bond strength for samples with various C_c and C_w at 28 and 90 curing days, respectively. The typical linear increase before the first crest comes from the combined effect of GFRP tendons and cemented soil mixtures, representing the elastic stage of the interface bond performance when experiencing initial slip behavior [67-69]. Clearly, increasing cement content would enhance the stiffness and bonding strength capacity of the whole innovative tendon-soil structure, possibly because of rising stabilizing hydration products. As slip continues, the interlock within tendon ribs and soil matrix is destroyed, and therefore the interface bond strength decline, reaching the first trough point where determines the residual strength. From Figs. 13 and 14, most curves experience fluctuations after the residual stage, owning the second peaking point. This phenomenon is related to the detached cement-soil fragments in consecutive ribs that accumulate and climb to the rib location, creating an additional slip-resistant plane when slippage proceeds. It is noteworthy that these strength fluctuations happen on bond-slip curves with high cement content, verifying the positive impact of cement addition. More detailed analysis of the progressive failure of tendon-cemented soil interface was demonstrated in the previous research by Chen, et al. (2020) [70].

Comparing results in Fig. 13 (a), (b) and (c), T_p shows a dramatic drop in the first and second peak points for samples when increasing the moisture content. For instance, sample C18W50T28 has a bond strength reaching 2015.96 and 763.94 kPa for crests, much higher than 395.29 and 131.19 kPa on sample C18W70T28. As for the curve of C18W90T28, the first crest owns 275.21 kPa while the second peak disappears. The possible explanation is the excess water causes pore pressures and weakens the structure, destroying the bonding performance. Unlike the negative influence of excess water, curing time T_c corresponds positively to the interface bonding relationship. Besides, 90-day samples exhibit greater peak strength values and extended slip elastic ranges than 28-day samples, which benefit from a prolonged cure period. It possibly comes from the sufficient hydration process producing adequate stabilizing products. In conclusion, both cement content and curing time are

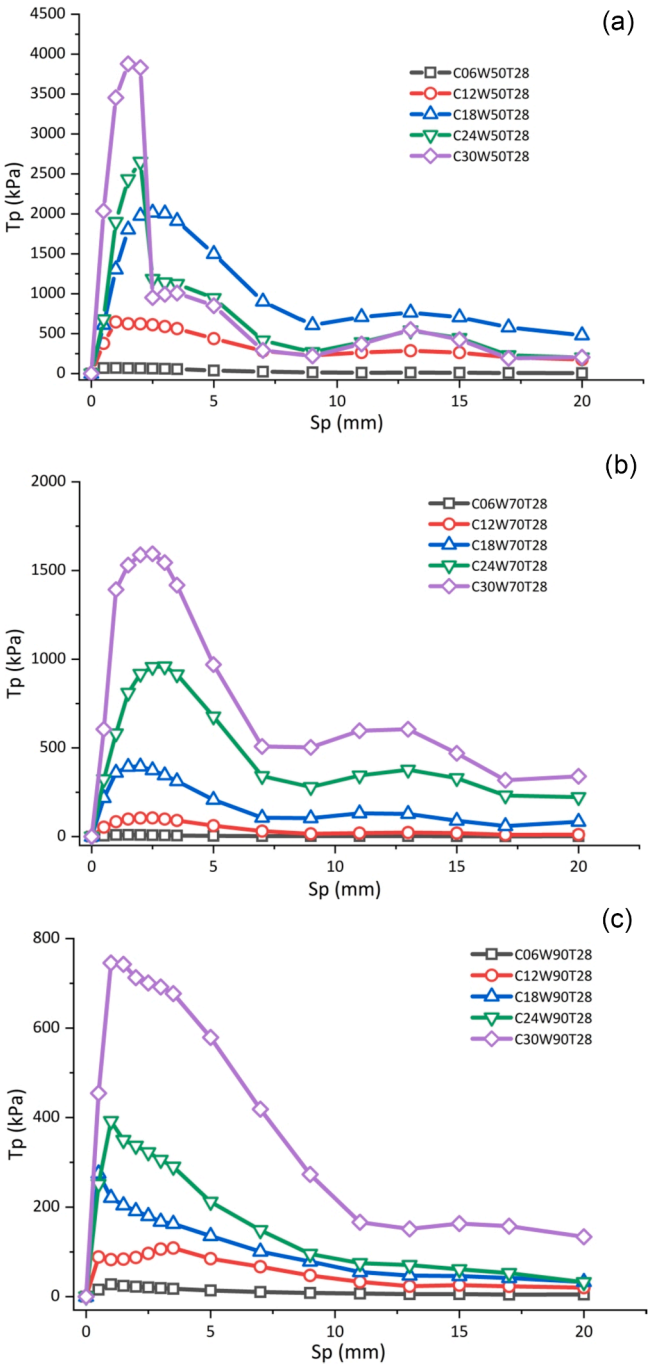

Fig. 13. The bond-slip curves specimens (28 day) with increasing C_c and (a) C_w: 50% (b) C_w: 70% (c) C_w: 90%

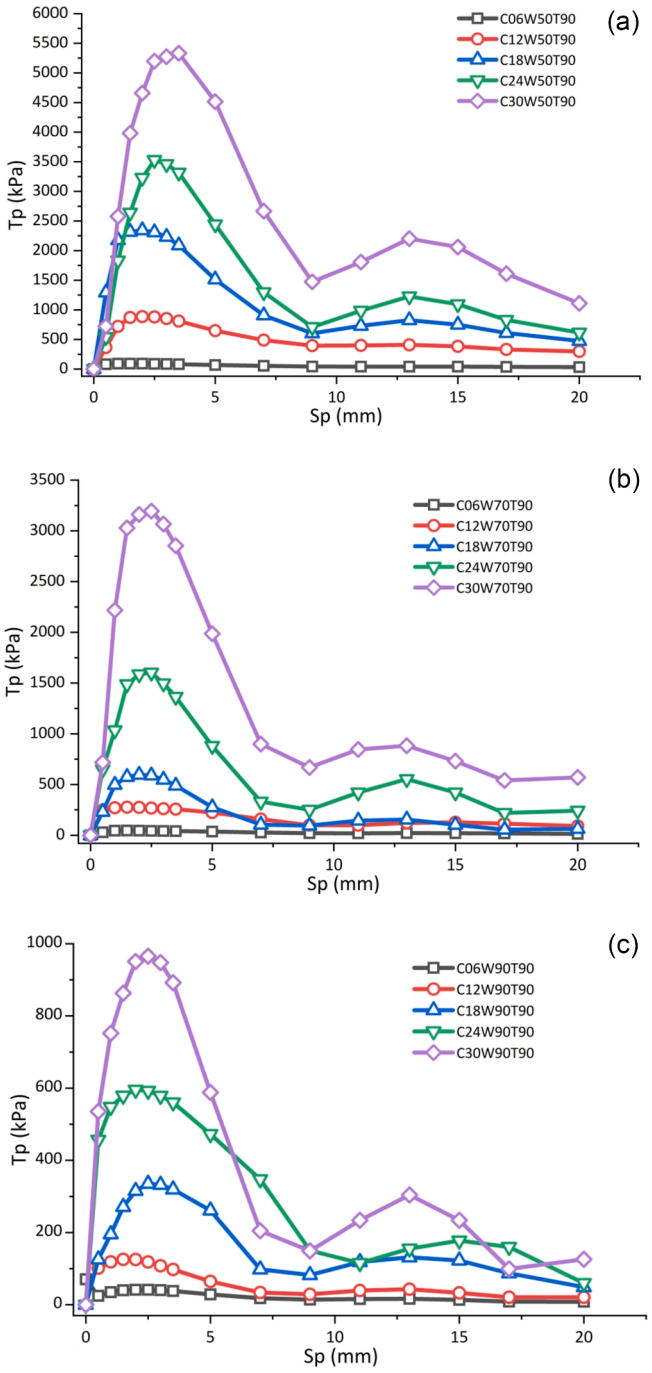

Fig. 14. The bond-slip curves specimens (90 days) with increasing C_c and (a) C_w: 50% (b) C_w: 70% (c) C_w: 90%

positively related to the GTRCS interface adhesion strength, converse to the water content in this study.

Regarding unconfined compressive strength, Fig. 15 illustrates the UCS of specimens that were prepared by combinations of different water and cement ratios and cured at two periods. With cement addition rising, the compressive strength witnesses a sharp improvement initially before the slow enhancement, like the ultimate interface bond strength. It also exhibits a similar decreasing trend as that of bonding performance when excess water was gradually introduced. Besides, extended curing time would result in better compression capacities of cement-soil samples by comparing Fig. 15(a) and (b). The mechanisms for the positive impacts of cement and curing time and the negative consequence of excess water on UCS are analogous to those for the pullout strength.

4.2. Modelling results

4.2.1. Results of hyperparameter tuning

Fig. 16 (a) indicates that the optimum hyperparameters should be chosen from the 1st fold among 10 cross-validations to run the SVR model based on the UCS dataset. This was attributed to the minimum RMSE value of fold 1. Fig. 17 (a) illustrates how the RMSE of the selection fold converges as iteration proceeds. The RMSE value of this fold declined dramatically initially, indicating the outstanding performance of BAS-SVR. The least figure was reached at the 46th iterations, and optimal hyperparameters were obtained with $C = 480343.30$ and $\gamma = 1.68$ for UCS prediction. A similar procedure applied for the T_p dataset. The selection fold was the 7th fold with the minimum RMSE, and iteration converged at the 35th times from Fig. 16 (b) and 16 (b). The corresponding hyperparameters of the BAS model for pullout strength estimation were $C = 256312.13$ and $\gamma = 11.18$.

4.2.2. Performance of BAS-SVR

Fig. 18 compares predicted mechanical values from adjusted BAS-SVR models and actual data for both sets, including the training and test set. The most clustering of test result points around the prediction line verified the reliability of the BAS-SVR model in predicting UCS. The correlation coefficients (R) for the training and test set were 0.9953 and 0.9879, as shown in Fig. 18 (a), which also proved the excellent performance of the tunned model. Comparing with the UCS estimation figure, it is noteworthy that more outlier points appeared in T_p predicted-actual graph away from the fitting line gathering the majority of experimental results. The possible reason is that T_p possessed relatively larger noise than UCS, which might be derived from the larger experimental errors since only one sample was conducted in the pullout test whereas three parallel samples were conducted in the UCS test. Besides, the limited dataset (especially when T_p value smaller than 10 kPa) will also be the influencing factor, causing larger scatter of the ratio of predicted T_p to actual T_p and even negative prediction values when actual T_p close to zero. However, this was supposed to be acceptable in the pullout strength simulation. From Fig. 18 (b), the corresponding correlation values were 0.987 and 0.972 for training as well as test sets, respectively, indicating the high accuracy of the BAS-SVR model. Close R values in both figures showed that no overfitting problems existed, indicating the effectiveness of cross validation. Apart from the R value, Table 7 summarises other evaluation indices of the BAS-SVR model performance for strength aspects, including RMSE, MAE, and MAPE.

4.2.3. GTRCS mixture optimisation

By using the MOBAS-SVR, the possible solutions can be found to minimize the objective function (maximise the T_p or UCS and simultaneously minimise the cost). The 20 non-dominated solutions for UCS-cost are obtained within the restrictions based on the dataset, as presented in Fig. 19. The widely distributed Pareto points can be observed in this figure with reasonable ranges of cost and UCS, illustrating the effectiveness of MOBAS-SVR in solving the bi-objective optimisation problem. The UCS is in positive relationship with cost. In Fig. 19, the minimum UCS and maximum UCS are 1158 and 9807 kPa, respectively, corresponding to the lowest (15.33 $/m^3) and highest cost (44.28 $/m^3) of GTRCS. Therefore, the balance between UCS and budget must be judged by the decision-maker. As mentioned before, the most suitable design solution can be automatically obtained through the TOPSIS approach. The point with the value of TOPSIS 1 shows the 9307 kPa UCS and 39.80 $/m3 cost. The corresponding cement and water content is 32.23% and 53.90%, respectively.

Regarding the bi-objective optimisation between cost and T_p, Fig. 20 presents the Pareto fronts for GTRCS. Besides, the influence of slip distance must be taken into account since it significantly affects the pullout strength as analysed before. Therefore, the relationships between cost and T_p under varying limitations of slip distance (5, 10, 15, 20 mm) are

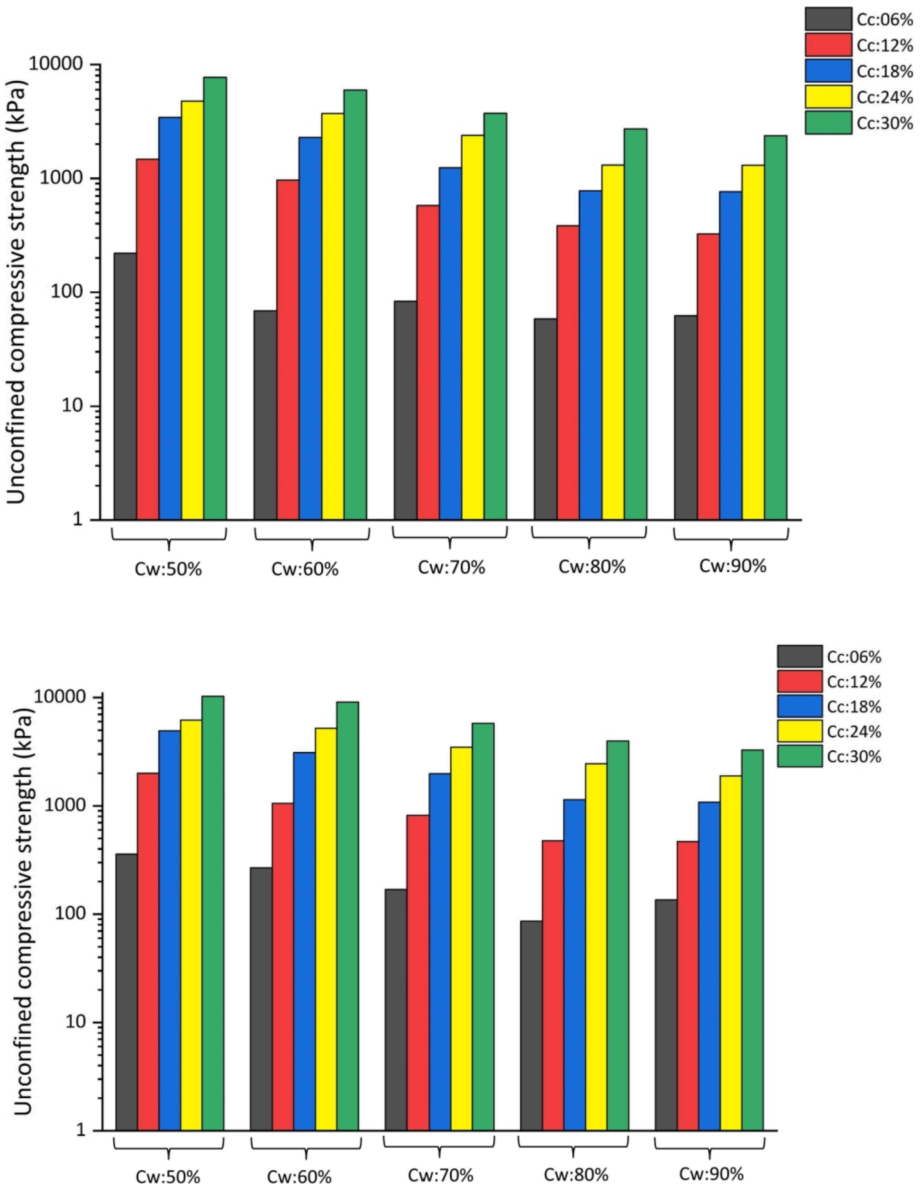

Fig. 15. The results for samples with various water and cement content under two cure periods (a) 28-day (b) 90-day.

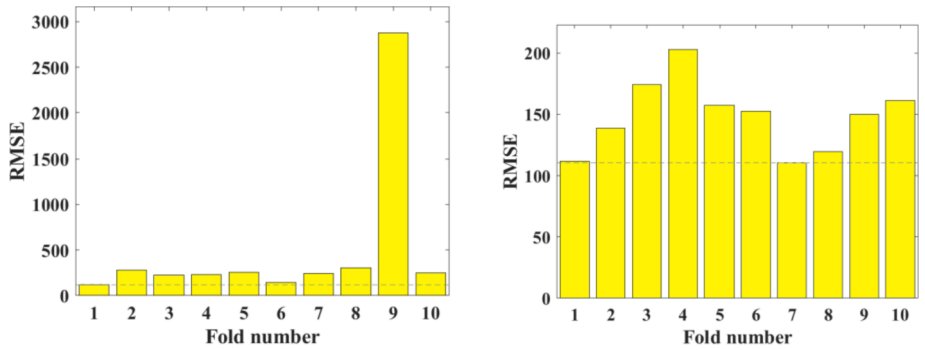

Fig. 16. RMSE of 10-fold CV for on the (a) UCS and (b) T_p dataset.

investigated through the MOBAS-SVR program. In total, five Pareto fronts based on the slip distance limitation are developed showing the similar relationship between cost and T_p. Specifically, the pullout strength can only be improved by increasing the cost of GTRCS. The pullout strength gradually decreases with the increase of slip distance except for the situation of 15 mm slip distance. This phenomenon agrees well with the laboratory tests results. Five points with the highest TOPSIS value corresponding to varying situations of slip distance are presented in Fig. 20. The corresponding mixture proportions of these

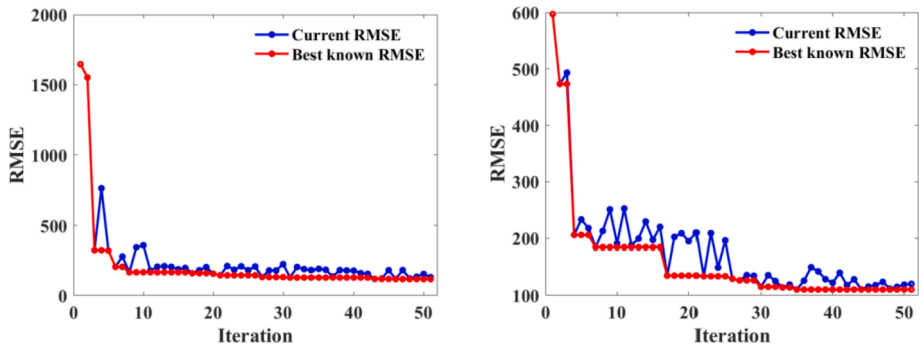

Fig. 17. RMSE iteration in the optimal fold of (a) UCS and (b)T_p

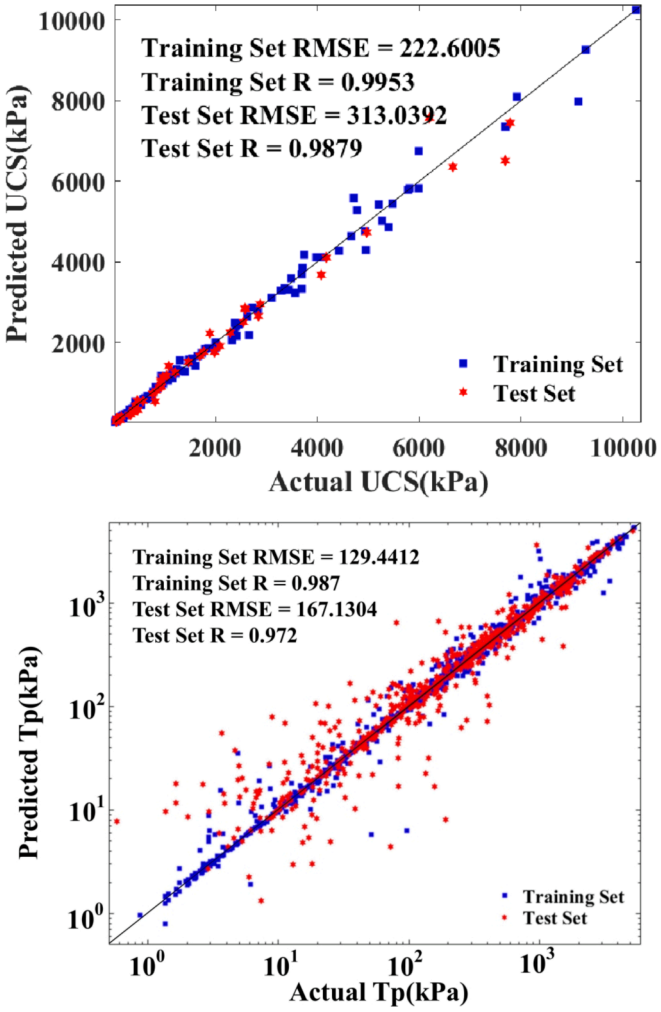

Fig. 18. Actual versus predicted values for (a) UCS (b) and.T_p

Table 7
Evaluation index of UCS and T_p modelling.

Test	Evaluation index			
	RMSE	R	MAE	MAPE
UCS (kPa)	313.039	0.988	170.901	0.145
T_p (kPa)	167.130	0.972	68.019	0.762 s

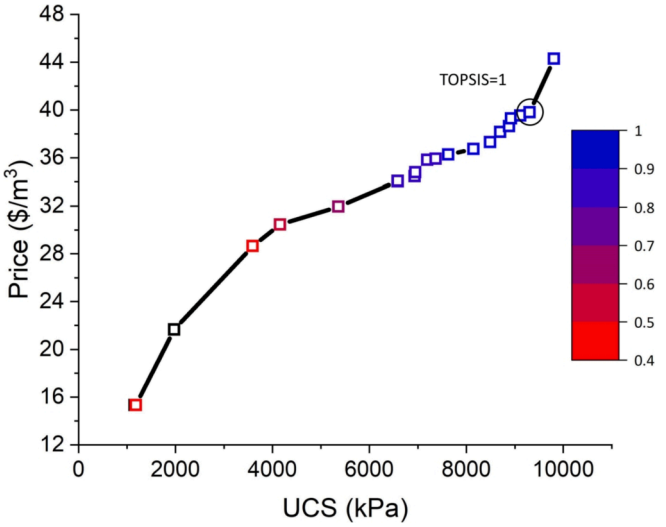

Fig. 19. Pareto fronts of cost and UCS for GTRCS.

designs are summarised in Table 8. In general, decision-makers should achieve the balance between the budget and desired mechanical performance. Otherwise, it is optimal to have the ideal solution with the highest TOPSIS.

4.2.4. *Variable significance*

The ranking importance of input variables for UCS and T_p of GTRCS is depicted in Fig. 21. For influential factors on the UCS, C_c owned the most significant value at 0.4736, which indicated its greater weight than the other two variables. Then followed by C_w with 0.3879, it was around 2.8 times higher than that of T_c (0.1386). A similar trend was observed in the T_p aspect, where C_c was 0.292, slightly higher than that of C_w (0.2777) and S_p (0.2615) in importance ratio. As for T_c, it influenced less around 0.1615 among these factors. This is mainly attributed to the less effect of curing time than cement/water ratio on strength at late stage (e.g., 90 days), which can be found on the strength evolution curve. In conclusion, C_c governed the mechanical strengths of GFRCS while T_c behaved inferior. Besides, S_p was also essential in the pullout behavior of GTRCS.

5. Conclusions

In this study, the compressive test and pullout test were conducted to investigate UCS and the interface bond strength between the cemented soil and GFRP tendons. Based on the laboratory tests results, the Pareto fronts for UCS-cost and T_p-cost were successfully achieved through proposing MOBAS-SVR. The main conclusions were depicted as follows.

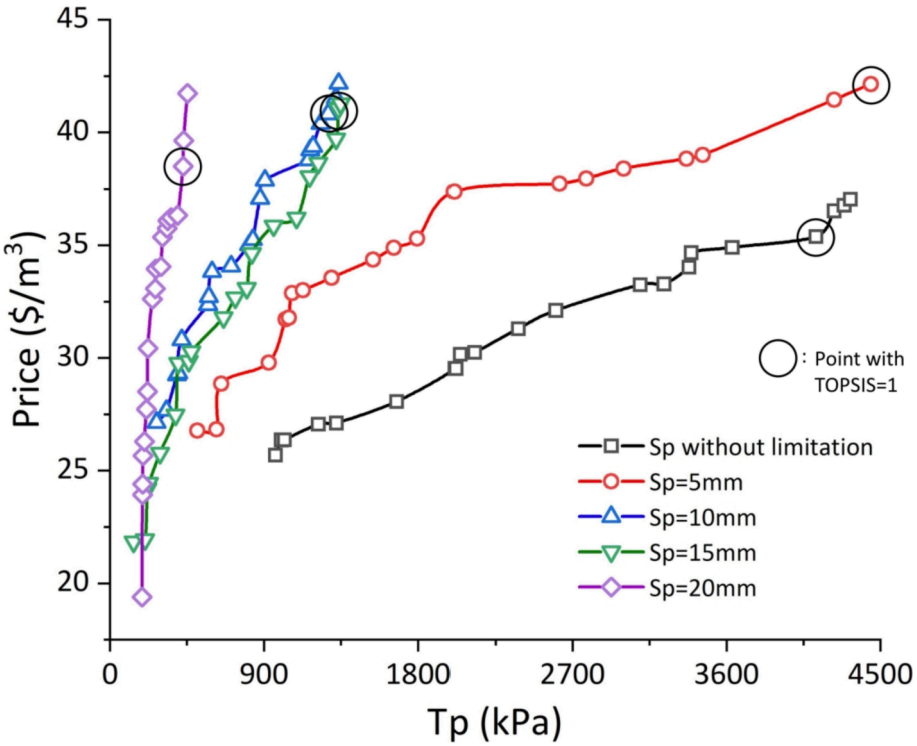

Fig. 20. Pareto fronts of cost and T_p for GTRCS.

Table 8
Mixture proportions of Pareto solutions of GTRCS.

Cc	Cw	Sp (mm)	T_p (kPa)	Cost ($/m^3)	TPOSIS
27.30%	59.70%	3.298	4122.23	35.38	1
28.59%	51.80%	5	4443.40	42.15	1
29.35%	55.70%	10	1320.82	41.54	1
25.51%	52.50%	15	1322.76	39.72	1
26.73%	60.10%	20	428.99	38.50	1

- The T_p and UCS were both positively related to the cement content and curing ages. However, the excessive water negatively affected the mechanical performance of GTRCS mainly due to the porous structure generalisation.
- The increased elastic phase and residual pullout strength can be observed on specimens with high cement to water ratio (high cement content or low water content) owing to improved robustness of GTRCS to withstand detachment of soil matrix.
- The BAS-SVR models were successfully established on both UCS and T_p datasets with high values of correlation coefficients (UCS: 0.988, T_p: 0.972) and low RMSE values (UCS: 313 kPa, T_p: 167 kPa). However, the proposed models have its specificity on the laboratory

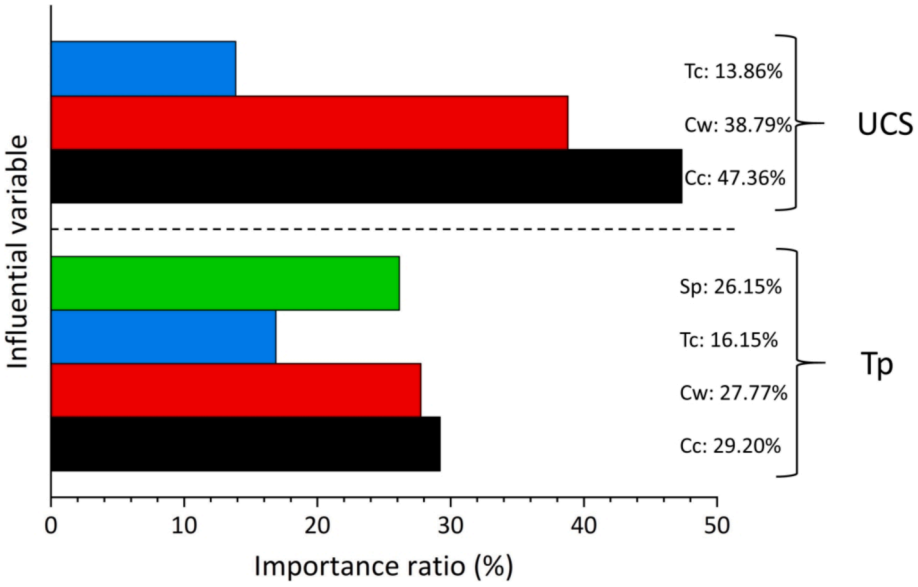

Fig. 21. The relative importance of each variable on UCS and T_p of GTRCS mixture optimisation.

data. The models must be revised according to the field data owing to the inevitable difference between the laboratory and field test results.

- The Pareto fronts for bi-objective optimisation (UCS-cost and T_p-cost) based on MOBAS-SVR were successfully obtained, providing feasible design solutions for decision-makers. Apart from the specific requirements, the solution with the highest TOPSIS is preferable.
- From sensitivity analysis, the cement content was the most significant influencing factor for both UCS and T_p, followed by water content. The curing time was of the least significance.

It is noted that only one type of cement and GFRP tendon are used in this study, inevitably affecting the generalisation performance of established models. The models are recommended to be adjusted by enlarging the database if the difference of the cement (or tendon) between others and the used one is significant. In the future, more possible influencing factors need to be investigated such as the tendon type, soil components, etc. Besides, the experimental investigation of the impact of bond length of GFRP tendon on the averaged bond strength is in progress. It is reported that the bond length-diameter ratio ranging from 5 to 8 is required to induce approximately uniform bond stress distribution along bond length (the requisite for element pullout test) for rockbolts [71,72].

CRediT authorship contribution statement

Genbao Zhang: Conceptualization, Methodology. **Changfu Chen:** Methodology, Formal analysis. **Kefei Li:** Formal analysis. **Fan Xiao:** Formal analysis. **Junbo Sun:** . **Yufei Wang:** Conceptualization, Methodology. **Xiangyu Wang:** Conceptualization, Supervision.

Declaration of Competing Interest

The authors declare that they have no known competing financial interests or personal relationships that could have appeared to influence the work reported in this paper.

Acknowledgements

This work was sponsored by the National Natural Science Foundation of China (grant numbers 51908201 and 51978254), Natural Science Foundation of Hunan Province (grant number 2020JJ5024), and the Key R&D Project of Hunan Province Intelligent Disaster Prevention and Mitigation and Ecological Restoration in Civil Engineering (grant number 2020SK2109). Meanwhile, this work was supported by Hunan Key Laboratory of Intelligent Disaster Prevention and Mitigation and Ecological Restoration in Civil Engineering, Hunan Provincial Engineering Research Center, Catastrophe and Reinforcement of Dangerous Engineering Structures. The research was also supported by Academic Research Council of Australia Linkage Projects for Asset Intelligence: Maximising Operational Effectiveness for Digital Era (grant number LP180100222).

Appendix

Specimen	Cc	Cw	Tc (day)	UCS (kPa)	Sp (mm)-Tp (kPa) 0.5	1	1.5	2	2.5	3	3.5	5	7	9	11	13	15	17	20
C06W50T07	0.06	0.50	7	186.43	46.24	53.50	51.08	48.12	45.17	42.48	38.71	28.50	18.28	11.02	11.83	11.56	9.68	8.60	6.18
C06W50T14	0.06	0.50	14	182.38	37.37	52.69	52.42	51.35	50.27	48.66	46.24	38.44	27.42	23.93	23.12	23.12	22.58	19.89	18.55
C06W50T28	0.06	0.50	28	219.86	68.95	70.31	67.59	65.68	62.95	59.96	56.14	38.43	23.16	14.72	10.63	11.45	9.81	7.36	5.72
C06W50T42	0.06	0.50	42	304.08	62.24	71.34	72.19	69.35	66.50	63.95	59.97	49.45	38.65	32.12	32.40	31.26	27.28	23.87	19.89
C06W50T60	0.06	0.50	60	337.41	73.21	78.52	79.05	78.52	76.66	74.01	71.62	62.34	45.36	36.08	35.01	35.54	34.22		
C06W50T90	0.06	0.50	90	358.50	82.14	91.23	91.80	91.23	89.24	86.11	81.85	68.78	54.57	42.63	40.93	41.21	40.93	37.23	33.25
C06W60T07	0.06	0.60	7	43.51	11.33	14.37	15.47	15.20	14.92	14.64	13.82	11.61	8.57	8.29	7.18	6.63	3.87	3.59	3.32
C06W60T14	0.06	0.60	14	54.54	2.56	3.41	4.55	5.97	6.25	7.11	7.39	6.82	4.83	3.41	3.98	3.69	3.41	2.84	2.56
C06W60T28	0.06	0.60	28	68.76	4.70	9.12	11.88	12.99	13.54	13.54	12.71	9.12	6.08	6.08	6.36	7.18	6.36	4.70	4.70
C06W60T42	0.06	0.60	42	108.82	41.34	49.09	46.51	43.92	43.92	43.92	41.34	33.59	23.25	20.67	20.67	20.67	18.09	12.92	10.33
C06W60T60	0.06	0.60	60	150.14	35.31	47.07	49.04	49.32	48.19	46.79	45.11	36.99	26.90	21.86	22.70	21.02	18.21	15.69	12.61
C06W60T90	0.06	0.60	90	268.37	43.88	45.51	45.51	45.78	45.24	44.42	42.79	37.34	30.52	24.53	24.25	23.16	20.71	17.71	13.90
C06W70T07	0.06	0.70	7	54.29	3.80	6.73	7.02	7.02	6.73	6.44	6.14	4.39	3.51	2.93	2.93	2.93	2.63	2.34	2.34
C06W70T14	0.06	0.70	14	70.80	7.21	9.70	9.95	9.70	8.95	8.46	7.71	4.23	2.49	3.73	2.98	3.23	2.74	1.99	2.49
C06W70T28	0.06	0.70	28	83.40	5.27	9.07	9.95	9.36	8.19	7.31	6.14	4.10	2.63	2.63	2.93	2.93	2.34	1.76	2.05
C06W70T42	0.06	0.70	42	130.82	16.58	27.35	30.12	30.95	30.39	29.29	28.46	25.14	17.96	14.09	9.39	12.16	11.61	9.67	7.46
C06W70T60	0.06	0.70	60	140.35	26.72	32.37	34.15	34.44	33.55	33.26	32.66	28.21	20.49	15.14	14.85	17.22	18.11	14.85	10.99
C06W70T90	0.06	0.70	90	169.46	29.22	44.76	46.63	44.76	43.21	41.96	40.72	36.68	27.35	19.89	19.27	21.14	20.52	18.03	13.68
C06W80T07	0.06	0.80	7	41.88	8.78	9.95	10.24	10.53	10.53	9.95	9.36	7.31	5.27	4.39	5.27	5.27	4.97	3.51	3.22
C06W80T14	0.06	0.80	14	52.65	1.36	1.64	2.18	2.73	3.00	3.00	3.00	2.73	2.18	1.36	1.36	1.64	1.64	1.36	1.36
C06W80T28	0.06	0.80	28	58.45	3.17	3.46	4.04	4.32	4.04	4.32	4.32	3.75	2.59	2.31	1.73	2.02	1.44	1.73	1.15
C06W80T42	0.06	0.80	42	61.46	10.76	12.07	12.39	11.41	10.11	9.13	8.15	5.87	4.89	2.94	3.26	2.28	1.96	1.63	0.98
C06W80T60	0.06	0.80	60	73.91	14.53	15.79	15.47	13.26	12.32	11.68	10.74	8.84	5.68	4.74	5.05	4.11	4.42	3.79	3.47
C06W80T90	0.06	0.80	90	86.26	8.31	12.77	13.36	13.06	12.47	11.88	11.88	9.50	5.94	5.05	5.05	5.05	4.45	3.86	3.56
C06W90T07	0.06	0.90	7	31.18	2.59	3.17	3.46	3.17	2.88	2.59	2.31	1.73	1.44	1.15	0.86	0.58	0.29	0.29	0.29
C06W90T14	0.06	0.90	14	52.87	28.18	26.80	24.87	23.21	21.28	19.89	17.96	16.03	14.64	10.78	11.88	11.33	9.95	10.22	8.57
C06W90T28	0.06	0.90	28	62.24	15.58	27.52	24.20	22.22	20.56	19.23	17.57	13.93	10.28	8.29	6.96	5.64	5.64	4.64	4.97
C06W90T42	0.06	0.90	42	120.39	21.42	28.77	26.32	22.65	19.89	17.14	15.00	8.88	5.20	4.90	6.12	5.82	4.90	3.67	4.90
C06W90T60	0.06	0.90	60	122.31	40.94	56.80	53.92	51.61	49.30	47.57	44.69	34.89	30.56	25.08	23.07	23.35	19.89	18.16	15.86
C06W90T90	0.06	0.90	90	136.26	24.58	34.82	40.08	41.54	41.54	40.37	38.03	28.67	18.14	14.34	15.80	16.38	13.46	8.78	8.48
C12W50T07	0.12	0.50	7	933.88	195.99	354.33	376.92	375.57	365.09	343.85	321.54	244.38	166.68	108.07	98.13	100.28	96.78	79.04	54.84
C12W50T14	0.12	0.50	14	1209.18	91.80	236.17	389.08	461.27	457.85	450.75	443.64	375.44	231.63	143.81	148.36	160.86	157.17	111.12	77.87
C12W50T28	0.12	0.50	28	1468.98	377.71	646.00	623.83	622.41	610.19	589.44	562.73	437.68	282.50	227.93	263.46	286.48	262.89	204.34	175.64
C12W50T42	0.12	0.50	42	1692.52	426.31	755.99	738.93	721.88	704.83	670.72	628.09	485.99	338.20	264.31	289.89	309.78	264.31	207.47	170.52
C12W50T60	0.12	0.50	60	1868.03	186.85	436.87	546.56	583.93	582.58	508.11	487.95	411.06	297.07	191.95	181.47	189.53	197.06	182.54	116.95
C12W50T90	0.12	0.50	90	2003.61	364.73	721.17	870.38	886.96	881.43	853.80	809.59	649.33	489.07	395.12	400.65	408.94	384.07	331.57	298.42
C12W60T07	0.12	0.60	7	623.95	200.10	259.49	264.10	262.38	257.47	248.54	238.16	190.58	127.44	83.04	81.60	91.11	92.84	74.96	60.55

(*continued on next page*)

(*continued*)

Specimen	Cc	Cw	Tc (day)	UCS (kPa)	Sp (mm)-Tp (kPa) 0.5	1	1.5	2	2.5	3	3.5	5	7	9	11	13	15	17	20
C12W60T14	0.12	0.60	14	835.46	143.18	270.12	274.60	272.36	272.64	267.59	257.51	217.44	149.63	87.14	77.62	87.14	93.31	79.02	44.27
C12W60T28	0.12	0.60	28	967.62	233.48	308.64	311.95	313.34	302.84	272.44	246.47	164.68	90.08	73.22	100.02	110.52	91.46	57.20	58.58
C12W60T42	0.12	0.60	42	933.33	108.31	256.97	326.05	319.97	303.94	303.94	268.57	208.34	138.16	103.06	114.39	119.64	106.93	83.72	73.22
C12W60T60	0.12	0.60	60	934.00	255.78	494.52	500.20	491.68	454.73	426.31	400.73	321.15	269.99	176.21	196.10	204.63	187.58	150.63	130.73
C12W60T90	0.12	0.60	90	1055.10	150.01	329.60	382.29	382.03	375.84	369.12	358.91	296.00	190.07	89.26	74.47	95.44	112.65	96.78	54.31
C12W70T07	0.12	0.70	7	354.08	38.87	62.13	75.90	76.52	72.23	66.72	58.15	36.42	26.32	28.46	32.44	32.14	23.87	20.20	21.73
C12W70T14	0.12	0.70	14	535.05	44.99	64.27	79.58	75.90	72.23	63.66	56.01	31.22	11.94	14.08	16.83	19.89	13.47	6.12	9.18
C12W70T28	0.12	0.70	28	577.55	52.95	83.67	98.89	104.45	105.03	98.89	90.99	61.44	31.01	15.80	19.89	22.82	19.60	10.53	11.41
C12W70T42	0.12	0.70	42	644.56	156.63	236.21	222.20	216.04	211.55	207.91	201.47	167.00	116.84	77.62	71.17	74.81	77.34	63.89	51.56
C12W70T60	0.12	0.70	60	668.03	265.45	269.71	273.12	272.55	272.27	268.86	262.32	226.51	160.01	90.66	79.29	100.04	111.69	99.19	61.39
C12W70T90	0.12	0.70	90	816.46	247.38	270.16	276.79	273.91	267.56	262.09	256.61	224.32	159.44	99.18	99.18	121.67	127.44	114.75	91.11
C12W80T07	0.12	0.80	7	209.93	20.47	23.64	27.68	29.41	29.70	27.68	23.64	9.80	5.48	4.90	6.63	6.63	3.46	2.02	2.88
C12W80T14	0.12	0.80	14	376.05	31.57	38.73	40.32	39.52	36.61	32.36	28.91	18.57	9.81	10.88	14.59	16.18	11.41	7.16	11.14
C12W80T28	0.12	0.80	28	384.45	31.26	47.46	47.46	46.04	44.34	42.35	39.22	23.87	8.53	7.39	11.65	15.35	12.51	5.68	7.11
C12W80T42	0.12	0.80	42	421.43	129.80	116.10	109.91	105.34	101.10	97.52	94.25	79.58	51.20	38.16	30.66	32.61	30.33	22.18	15.33
C12W80T60	0.12	0.80	60	432.93	40.38	98.28	126.20	120.55	112.24	104.52	97.69	75.12	56.12	37.41	32.66	33.55	29.99	25.83	20.79
C12W80T90	0.12	0.80	90	477.01	144.09	134.14	128.46	121.07	116.81	112.26	106.29	87.82	63.95	43.77	36.95	32.40	28.70	28.99	24.16
C12W90T07	0.12	0.90	7	161.77	9.44	23.21	31.37	32.39	31.63	29.59	27.04	18.11	14.03	14.54	17.34	15.81	11.22	8.93	9.95
C12W90T14	0.12	0.90	14	260.76	86.84	74.52	66.31	60.31	53.68	47.37	43.26	33.47	26.84	17.37	17.05	12.63	15.47	13.89	13.26
C12W90T28	0.12	0.90	28	324.08	88.57	82.85	83.67	87.48	96.47	106.28	108.47	84.76	66.77	47.42	32.98	23.44	25.62	23.16	20.17
C12W90T42	0.12	0.90	42	410.78	65.37	76.17	108.57	144.66	168.82	169.67	162.85	125.05	66.79	26.43	29.56	38.65	32.12	24.73	19.04
C12W90T60	0.12	0.90	60	429.24	82.34	98.09	135.39	167.44	170.48	168.83	157.22	103.06	46.70	17.68	25.70	31.78	27.35	21.28	11.33
C12W90T90	0.12	0.90	90	469.25	101.23	118.61	125.66	125.41	118.36	108.03	97.71	64.72	33.74	28.96	39.54	43.06	32.74	20.65	20.90
C18W50T07	0.18	0.50	7	2469.45	459.48	649.16	674.23	683.22	674.77	636.07	569.03	388.35	234.37	206.85	227.83	226.20	181.50	135.72	129.45
C18W50T14	0.18	0.50	14	2580.66	817.58	1381.70	1482.54	1501.62	1482.54	1436.21	1359.90	1060.12	596.83	463.29	547.78	588.66	501.45	337.93	280.70
C18W50T28	0.18	0.50	28	3431.97	610.09	1305.07	1803.76	1976.17	2015.96	2005.35	1912.51	1498.71	901.88	607.44	708.24	763.94	705.59	578.26	480.12
C18W50T42	0.18	0.50	42	4075.51	997.41	1887.28	2056.65	2123.86	2118.48	2053.96	1951.80	1411.42	825.35	521.56	688.24	774.27	674.80	513.49	424.77
C18W50T60	0.18	0.50	60	4432.27	806.68	1626.98	2093.00	2133.88	2147.50	2122.97	2035.77	1547.95	970.19	610.46	730.37	817.58	768.52	618.63	476.92
C18W50T90	0.18	0.50	90	4931.29	1293.13	2177.63	2317.43	2344.31	2309.36	2234.08	2088.91	1513.59	908.69	604.90	731.25	825.35	750.07	610.27	475.85
C18W60T07	0.18	0.60	7	1546.43	470.74	495.96	495.96	487.55	473.54	451.13	425.91	358.66	308.22	302.62	288.61	280.20	252.18	235.37	221.36
C18W60T14	0.18	0.60	14	2085.78	385.69	640.60	652.00	633.70	608.50	579.06	542.72	391.79	214.33	171.62	209.55	226.80	189.66	122.02	106.10
C18W60T28	0.18	0.60	28	2291.43	739.73	1165.64	1140.42	1109.60	1056.36	997.52	935.88	689.30	403.49	299.82	358.66	361.46	319.43	252.18	218.56
C18W60T42	0.18	0.60	42	2548.09	1022.35	1558.39	1646.81	1613.65	1608.13	1569.44	1514.18	1199.19	734.99	356.44	323.28	431.04	461.44	364.73	140.92
C18W60T60	0.18	0.60	60	2878.23	843.52	1469.53	1530.54	1488.10	1429.74	1342.21	1246.71	923.10	557.04	435.02	551.74	562.35	485.42	371.36	331.57
C18W60T90	0.18	0.60	90	3098.16	1040.19	1614.29	1659.76	1642.71	1617.13	1531.87	1435.24	1040.19	417.78	386.52	525.78	596.83	517.25	355.26	312.63
C18W70T07	0.18	0.70	7	898.78	184.23	277.16	293.51	285.33	276.61	267.62	255.63	201.12	120.18	55.87	53.96	76.03	79.03	62.95	26.16
C18W70T14	0.18	0.70	14	1157.21	206.55	291.39	327.38	346.10	345.23	327.96	301.34	192.51	98.59	96.55	134.29	143.36	98.89	53.83	64.95
C18W70T28	0.18	0.70	28	1243.20	217.11	360.12	393.56	395.29	374.24	345.99	312.26	207.88	106.39	103.80	131.19	127.73	89.67	59.68	83.61
C18W70T42	0.18	0.70	42	1506.12	258.34	442.51	484.57	489.69	472.63	433.13	395.05	250.10	103.17	98.90	162.85	180.19	131.59	65.37	87.54
C18W70T60	0.18	0.70	60	1802.99	137.27	293.02	466.95	521.23	528.91	514.13	486.56	343.89	144.66	117.66	186.72	214.01	173.37	96.06	93.50
C18W70T90	0.18	0.70	90	1983.95	231.17	496.80	575.26	596.83	589.83	547.80	488.95	276.56	104.80	95.83	144.58	154.95	102.83	55.48	63.61
C18W80T07	0.18	0.80	7	505.65	34.10	62.24	67.64	66.50	62.81	56.84	51.44	32.12	19.04	20.46	27.28	25.01	17.34	12.22	19.04
C18W80T14	0.18	0.80	14	744.76	132.05	168.38	176.45	170.69	160.60	149.64	138.68	105.81	69.49	32.87	27.68	29.99	28.83	27.10	14.99
C18W80T28	0.18	0.80	28	776.53	76.91	116.10	136.89	142.82	142.23	134.21	123.52	72.75	26.13	29.40	41.87	46.62	31.18	16.63	19.30
C18W80T42	0.18	0.80	42	936.05	172.42	283.49	298.42	303.06	306.70	304.38	296.76	253.98	178.05	114.06	113.73	128.98	126.66	112.40	91.85
C18W80T60	0.18	0.80	60	1039.52	320.84	299.68	296.52	287.36	279.78	265.26	253.26	197.05	142.10	110.21	103.89	98.52	93.16	85.58	65.05
C18W80T90	0.18	0.80	90	1142.72	290.92	309.95	290.92	284.00	284.00	269.87	258.05	221.72	153.39	110.14	97.45	91.98	92.84	73.23	61.41
C18W90T07	0.18	0.90	7	421.02	67.75	147.06	183.89	165.88	155.12	147.86	142.49	126.62	101.89	62.64	48.39	48.66	50.27	47.85	38.44
C18W90T14	0.18	0.90	14	586.75	231.53	192.77	180.42	171.50	167.73	160.18	152.29	127.94	101.53	80.26	78.89	82.66	83.01	81.64	67.23
C18W90T28	0.18	0.90	28	763.88	275.21	220.83	204.25	191.32	180.04	167.44	162.80	135.61	100.80	78.58	55.04	47.08	46.09	41.45	32.83
C18W90T42	0.18	0.90	42	863.06	137.56	248.40	305.80	326.27	310.35	292.16	269.14	191.84	102.31	59.40	74.75	80.43	73.04	41.78	30.41
C18W90T60	0.18	0.90	60	969.22	117.97	194.18	262.83	297.01	303.74	287.49	272.64	162.80	73.13	48.76	70.33	77.06	59.40	35.31	29.70
C18W90T90	0.18	0.90	90	1083.40	125.51	195.43	271.21	315.68	335.28	332.35	319.48	261.26	98.01	82.21	118.49	131.65	122.58	87.18	48.86
C24W50T07	0.24	0.50	7	4176.33	853.01	1700.56	1760.52	1735.99	1670.58	1599.73	1466.19	1046.50	645.89	564.13	664.96	703.12	610.46	479.65	427.87
C24W50T14	0.24	0.50	14	4666.67	814.59	1707.15	2317.43	2277.10	2158.81	2083.53	1970.62	1537.78	981.28	731.25	822.66	865.67	836.10	680.17	623.72
C24W50T28	0.24	0.50	28	4770.39	679.72	1898.25	2434.30	2652.58	1185.37	1141.16	1121.82	944.98	414.47	268.02	392.36	538.81	444.86	229.34	201.71
C24W50T42	0.24	0.50	42	5817.69	908.00	3083.63	3466.21	1349.25	1517.58	1678.27	1747.13	1706.32	976.86	308.62	517.76	905.45	925.85	642.74	278.01
C24W50T60	0.24	0.50	60	5979.59	664.04	1922.23	2513.68	2664.23	2771.77	2734.13	2594.33	1992.13	1113.01	588.77	795.77	967.83	908.69	677.48	440.90
C24W50T90	0.24	0.50	90	6197.96	540.79	1832.52	2639.51	3227.93	3530.55	3460.50	3314.79	2443.36	1297.34	708.91	986.31	1227.29	1095.59	829.40	616.45
C24W60T07	0.24	0.60	7	2585.33	1045.15	1165.64	1148.83	1123.61	1098.39	1070.37	1019.94	818.19	602.44	574.41	549.20	568.81	532.38	386.68	372.67
C24W60T14	0.24	0.60	14	3297.28	1026.13	1518.25	1633.43	1628.20	1581.08	1473.75	1355.96	900.48	429.30	376.95	502.59	557.57	416.21	253.91	280.09
C24W60T28	0.24	0.60	28	3708.16	357.56	1037.73	1820.07	2099.66	2037.83	1879.21	1793.18	1457.13	809.22	491.98	631.78	723.19	701.68	551.13	491.98
C24W60T42	0.24	0.60	42	4948.98	659.36	1818.91	2304.90	2543.64	2626.06	2586.27	2503.85	1975.23	1105.56	593.99	804.30	1020.30	954.93	707.67	460.41
C24W60T60	0.24	0.60	60	5272.79	891.16	2300.12	2608.07	2831.54	2883.32	2777.04	2567.19	1978.54							
C24W60T90	0.24	0.60	90	5212.24	615.65	1661.45	2341.62	2672.30	2852.42	2825.54	2720.69	2191.07	1220.55	626.40	838.79	1024.29	975.90	763.51	610.27
C24W70T07	0.24	0.70	7	1654.22	324.75	468.10	494.43	491.51	485.66	462.25	424.22	310.12	198.94	193.09	239.90	234.05	190.17	140.43	160.91
C24W70T14	0.24	0.70	14	2319.09	350.25	577.22	711.71	753.74	731.33	700.51	636.06	437.12	215.76	187.74	268.99	288.61	224.16	126.09	140.10
C24W70T28	0.24	0.70	28	2383.27	323.65	581.98	810.62	917.52	956.12	959.09	914.55	677.00	341.47	279.12	344.44	377.10	329.59	231.61	222.70
C24W70T42	0.24	0.70	42	2837.41	792.85	1380.90	1462.82	1480.38	1454.04	1410.16	1369.20	1170.26	772.37	427.14	456.40	535.39	558.80	468.10	365.71
C24W70T60	0.24	0.70	60	3353.06	669.97	1228.77	1515.48	1571.07	1550.59	1465.75	1339.94	789.92	283.79	301.34	535.39	558.80	359.85	178.46	275.01
C24W70T90	0.24	0.70	90	3478.23	648.73	1035.08	1487.75	1585.78	1603.08	1496.40	1363.77	879.39	331.57	250.84	420.95	553.58	420.95	219.13	242.19
C24W80T07	0.24	0.80	7	822.31	44.11	119.94	167.52	187.99	191.74	182.22	160.31	89.96	47.00	56.80	76.41	81.31	53.34	31.43	45.56
C24W80T14	0.24	0.80	14	1228.30	185.59	207.75	212.59	212.02	207.19	199.51	190.70	161.71	126.47	97.48	93.50	88.96	79.29	70.20	55.99
C24W80T28	0.24	0.80	28	1309.97	307.90	321.06	323.21	322.59	313.72	305.76	293.21	240.87	170.17	116.61	111.10	126.71	117.22	98.55	75.90
C24W80T42	0.24	0.80	42	1983.67	298.42	653.84	676.71	678.78	681.75	671.06	652.36	562.39	393.73	203.99	177.56	216.17	229.53	199.54	119.07

(*continued on next page*)

(*continued*)

Specimen	Cc	Cw	Tc (day)	UCS (kPa)	Sp (mm)-Tp (kPa) 0.5	1	1.5	2	2.5	3	3.5	5	7	9	11	13	15	17	20
C24W80T60	0.24	0.80	60	2425.65	678.75	833.81	845.51	851.36	851.36	839.66	816.25	731.41	511.99	289.64	245.75	260.38	289.64	251.61	160.91
C24W80T90	0.24	0.80	90	2448.98	1055.93	1156.93	1184.48	1172.24	1141.63	1101.84	1052.87	853.93	501.95	214.25	260.16	345.86	361.16	269.34	168.34
C24W90T07	0.24	0.90	7	781.36	82.42	107.48	150.37	177.76	188.87	190.68	174.40	106.71	52.45	52.71	80.61	93.53	61.23	35.65	53.48
C24W90T14	0.24	0.90	14	1059.83	159.15	336.78	283.07	271.13	262.32	256.35	248.11	209.74	155.74	100.61	88.10	82.42	74.75	70.48	51.73
C24W90T28	0.24	0.90	28	1305.10	251.50	392.25	349.78	337.02	322.47	305.54	290.10	211.71	148.47	95.31	74.83	70.67	61.17	52.56	32.37
C24W90T42	0.24	0.90	42	1607.55	333.31	473.49	507.15	518.48	497.67	479.61	459.71	369.73	203.53	110.49	139.87	162.52	167.42	141.40	127.63
C24W90T60	0.24	0.90	60	1734.35	229.34	323.28	444.86	524.99	569.20	569.20	524.99	350.91	132.63	91.18	165.79	190.65	168.55	80.13	77.37
C24W90T90	0.24	0.90	90	1891.84	456.68	547.84	579.02	595.35	592.38	578.72	560.31	472.71	347.41	150.25	115.51	155.29	177.56	160.05	59.68
C30W50T07	0.30	0.50	7	4715.90	673.27	1367.74	1634.74	1758.03	1803.06	1788.66	1739.45	1391.30	895.25	620.65	657.82	733.74	673.53	570.39	438.98
C30W50T14	0.30	0.50	14	6657.82	863.02	1882.96	2591.87	2989.76	2967.34	2802.02	2247.22	585.62	439.92	297.01	353.05	437.12	448.32	316.63	271.80
C30W50T28	0.30	0.50	28	7695.24	2035.14	3454.63	3879.40	3831.01	951.70	992.03	1008.16	849.54	290.35	220.45	371.00	551.13	424.77	190.88	204.32
C30W50T42	0.30	0.50	42	7916.33	1802.20	2817.39	3744.82	4169.04	4300.69	4286.07	4069.57	3054.37	1796.34	933.28	1161.48	1521.33	1369.20	1123.45	687.53
C30W50T60	0.30	0.50	60	9260.82	1049.98	1867.86	2738.24	3650.06	4105.98	4329.79	4277.29	3216.26	1630.23	986.43	1279.32	1602.60	1508.66	1096.95	898.01
C30W50T90	0.30	0.50	90	10255.10	722.92	2577.86	3981.68	4659.77	5197.75	5273.41	5332.25	4514.06	2667.53	1473.86	1807.31	2202.39	2059.49	1611.16	1109.60
C30W60T07	0.30	0.60	7	4104.90	1520.50	1591.55	1611.44	1585.87	1546.08	1546.08	1423.87	1159.56	881.04	761.67	767.35	773.04	687.78	622.41	588.30
C30W60T14	0.30	0.60	14	5389.29	681.31	1558.85	2090.27	2221.08	2172.03	2114.80	2008.51	1376.25	656.79	517.80	673.14	741.27	577.75	386.99	365.18
C30W60T28	0.30	0.60	28	5980.95	1530.76	2550.35	2995.21	3188.63	3207.97	3116.78	2876.39	2025.36	1049.98	801.30	1005.77	1083.14	978.14	754.33	679.72
C30W60T42	0.30	0.60	42	7687.07	1166.78	3360.54	4169.75	4309.55	4167.06	3933.17	3648.20	2795.97	1836.20	1250.12	1419.49	1481.32	1360.34	1139.89	986.65
C30W60T60	0.30	0.60	60	7782.31	1225.49	2864.79	4063.76	4323.71	2774.60	2533.22	2363.45	1883.33							
C30W60T90	0.30	0.60	90	9115.65	976.15	2140.63	2801.13	3626.08	4016.01	4063.76	4018.66	2984.16	1702.96	901.88	1225.49	1450.96	1273.24	946.97	782.51
C30W70T07	0.30	0.70	7	2621.32	257.30	480.12	753.33	981.46	1010.63	1002.68	968.19	753.33	456.24	307.70	366.06	397.89	352.79	241.39	190.99
C30W70T14	0.30	0.70	14	3689.12	557.04	1179.45	1349.97	1421.03	1429.55	1367.03	1267.56	971.98	548.52	457.57	557.04	562.73	500.20	375.15	397.89
C30W70T28	0.30	0.70	28	3732.65	605.12	1392.61	1530.76	1588.79	1594.31	1544.58	1417.47	969.85	508.41	502.89	596.83	605.12	469.73	317.76	339.86
C30W70T42	0.30	0.70	42	4969.39	767.75	1852.14	2350.90	2488.20	2541.44	2485.40	2437.76	2174.37	1479.47	549.20	439.92	745.34	896.65	736.93	459.53
C30W70T60	0.30	0.70	60	5480.27	900.62	1771.67	2244.84	2551.32	2672.30	2629.28	2476.04	1744.79	760.83	481.23	698.99	881.80	685.55	403.26	
C30W70T90	0.30	0.70	90	5780.27	718.57	2218.07	3028.69	3162.31	3194.98	3067.30	2853.51	1986.47	899.70	668.09	846.25	881.88	730.45	540.41	570.11
C30W80T07	0.30	0.80	7	1481.50	192.95	480.46	608.82	639.89	626.54	605.82	569.58	388.35	206.85	177.14	223.20	232.74	188.59	148.25	
C30W80T14	0.30	0.80	14	2660.45	778.48	983.19	1032.20	1058.15	1046.62	1032.20	1000.48	836.14	539.17	334.46	363.29	444.02	449.79	343.11	276.79
C30W80T28	0.30	0.80	28	2720.88	1068.17	1046.75	1028.39	991.66	967.17	936.57	896.78	743.74	517.25	400.95	373.40	370.34	355.04	321.37	278.52
C30W80T42	0.30	0.80	42	3568.71	491.83	958.80	1224.06	1326.29	1329.05	1276.56	1201.95	853.80	361.97	254.21	397.89	422.76	361.97	234.86	218.29
C30W80T60	0.30	0.80	60	3693.83	1348.40	1642.07	1673.65	1692.60	1714.71	1698.92	1648.39	1439.97	994.72	533.67	476.83	581.04	606.30	489.46	274.73
C30W80T90	0.30	0.80	90	3977.55	1597.67	1762.95	1851.71	1870.07	1860.89	1805.80	1735.40	1493.61	991.66	517.25	483.59	633.56	722.32	612.13	413.19
C30W90T07	0.30	0.90	7	1398.98	291.13	418.34	474.66	490.07	489.23	479.71	463.73	397.89	291.41	185.21	192.50	224.72	227.52	203.99	153.83
C30W90T14	0.30	0.90	14	1768.91	145.89	198.28	304.72	355.45	365.39	349.48	313.34	161.81	40.45	25.20	51.06	72.28	51.06	15.58	12.60
C30W90T28	0.30	0.90	28	2373.95	454.30	745.30	742.33	712.63	700.76	691.85	677.00	579.02	418.67	273.18	166.28	151.43	163.31	157.37	133.62
C30W90T42	0.30	0.90	42	2400.32	301.93	490.92	643.06	704.20	726.14	702.15	650.08	357.81	122.29	99.76	165.59	214.74	157.11	72.26	73.14
C30W90T60	0.30	0.90	60	2842.18	522.23	951.20	1103.52	1153.25	1125.28	1044.45	954.31	742.93	391.67	285.98	388.56	401.00	363.69	276.66	251.79
C30W90T90	0.30	0.90	90	3283.40	535.39	751.89	863.06	950.83	965.46	947.91	892.32	588.05	204.79	149.21	234.05	304.27	234.05	99.47	125.80

References

[1] J. Sun, Y. Wang, S. Liu, A. Dehghani, X. Xiang, J. Wei, X. Wang, Mechanical, chemical and hydrothermal activation for waste glass reinforced cement, Constr. Build. Mater. 301 (2021) 124361, https://doi.org/10.1016/j.conbuildmat.2021.124361.

[2] A. Dehghani, F. Aslani, N. Ghaebi Panah, Effects of initial SiO2/Al2O3 molar ratio and slag on fly ash-based ambient cured geopolymer properties, Constr. Build. Mater. 293 (2021) 123527, https://doi.org/10.1016/j.conbuildmat.2021.123527.

[3] F. Aslani, A. Dehghani, L. Wang, The effect of hollow glass microspheres, carbon nanofibers and activated carbon powder on mechanical and dry shrinkage performance of ultra-lightweight engineered cementitious composites, Constr. Build. Mater. 280 (2021) 122415, https://doi.org/10.1016/j.conbuildmat.2021.122415.

[4] J. Li, et al., Mechanical and conductive performance of electrically conductive cementitious composite using graphite, steel slag, and GGBS, Structural Concrete (2020).

[5] D.-S. Xu, M. Huang, Y. Zhou, One-dimensional compression behavior of calcareous sand and marine clay mixtures, Int. J. Geomech. 20 (9) (2020) 04020137, https://doi.org/10.1061/(ASCE)GM.1943-5622.0001763.

[6] 147, C., *Technical specification for soil mass with reinforced cement soil pile and anchors*. 2016: China Planning Press, Beijing, China.

[7] M. Abedini, C. Zhang, Dynamic vulnerability assessment and damage prediction of RC columns subjected to severe impulsive loading, Struct. Eng. Mechan. 77 (4) (2021) 441–461, https://doi.org/10.12989/sem.2021.77.4.441.

[8] Y. Du, N. Pan, Z. Xu, F. Deng, Y.u. Shen, H. Kang, Pavement distress detection and classification based on YOLO network, Int. J. Pavement Eng. 22 (13) (2021) 1659–1672, https://doi.org/10.1080/10298436.2020.1714047.

[9] Y. Tang, W. Feng, Z. Chen, Y. Nong, S. Guan, J. Sun, Fracture behavior of a sustainable material: Recycled concrete with waste crumb rubber subjected to elevated temperatures, J. Cleaner Prod. 318 (2021) 128553, https://doi.org/10.1016/j.jclepro.2021.128553.

[10] C. Chen, G. Zhang, J.G. Zornberg, A.M. Morsy, S. Zhu, H. Zhao, Interface behavior of tensioned bars embedded in cement-soil mixtures, Constr. Build. Mater. 186 (2018) 840–853.

[11] H. Huang, M. Huang, W. Zhang, S. Yang, Experimental study of predamaged columns strengthened by HPFL and BSP under combined load cases, Struct. Infrastruct. Eng. 17 (9) (2021) 1210–1227, https://doi.org/10.1080/15732479.2020.1801768.

[12] J. Sun, F. Aslani, J. Wei, X. Wang, Electromagnetic absorption of copper fiber oriented composite using 3D printing, Constr. Build. Mater. 300 (2021) 124026, https://doi.org/10.1016/j.conbuildmat.2021.124026.

[13] J. Sun, F. Aslani, J. Lu, L. Wang, Y. Huang, G. Ma, Fresh and mechanical behaviour of developed fibre-reinforced lightweight engineered cementitious composites for 3D concrete printing containing hollow glass microspheres, Ceram. Int. 47 (19) (2021) 27107–27121.

[14] J. Xu, Z. Wu, H. Chen, L. Shao, X. Zhou, S. Wang, Triaxial shear behavior of basalt fiber-reinforced loess based on digital image technology, KSCE J. Civ. Eng. 25 (10) (2021) 3714–3726, https://doi.org/10.1007/s12205-021-2034-1.

[15] Tepfers, R., et al., Bond of reinforcement in concrete. "Bond of reinforcement in concrete", 2000.

[16] Y. Ju, T. Shen, D. Wang, Bonding behavior between reactive powder concrete and normal strength concrete, Constr. Build. Mater. 242 (2020) 118024, https://doi.org/10.1016/j.conbuildmat.2020.118024.

[17] W. Zhang, Z. Tang, Y. Yang, J. Wei, P. Stanislav, Mixed-Mode Debonding Behavior between CFRP Plates and Concrete under Fatigue Loading, J. Struct. Eng. 147 (5) (2021) 04021055, https://doi.org/10.1061/(ASCE)ST.1943-541X.0003032.

[18] J. Sun, S. Lin, G. Zhang, Y. Sun, J. Zhang, C. Chen, A.M. Morsy, X. Wang, The effect of graphite and slag on electrical and mechanical properties of electrically conductive cementitious composites, Constr. Build. Mater. 281 (2021) 122606, https://doi.org/10.1016/j.conbuildmat.2021.122606.

[19] Timoney, M.J. and B.A.J.C.G.J. Mccabe, Strength Verification of Stabilised Soil-Cement Columns: A Laboratory Investigation of the Push-In Resistance Test (PIRT). **2017**, cgj-2016-0230.

[20] J. Sun, Y. Huang, F. Aslani, X. Wang, G. Ma, Mechanical enhancement for EMW-absorbing cementitious material using 3D concrete printing. J. Build. Eng. 41 (2021) 102763, https://doi.org/10.1016/j.jobe.2021.102763.

[21] F. Aslani, A. Deghani, Z. Asif, Development of lightweight rubberized geopolymer concrete by using polystyrene and recycled crumb-rubber aggregates, J. Mater. Civ. Eng. 32 (2) (2020) 04019345, https://doi.org/10.1061/(ASCE)MT.1943-5533.0003008.

[22] A. Dehghani, A. Hayatdavoodi, F. Aslani, The ultimate shear capacity of longitudinally stiffened steel-concrete composite plate girders, J. Constr. Steel Res. 179 (2021) 106550, https://doi.org/10.1016/j.jcsr.2021.106550.

[23] A. Hayatdavoodi, A. Dehghani, F. Aslani, F. Nateghi-Alahi, The development of a novel analytical model to design composite steel plate shear walls under eccentric shear, J. Build. Eng. 44 (2021) 103281, https://doi.org/10.1016/j.jobe.2021.103281.

[24] A. Dehghani, A.R. Mozafari, F. Aslani, Evaluation of the efficacy of using engineered cementitious composites in RC beam-column joints, Structures 27 (2020) 151–162.

[25] F. Aslani, A. Deghani, Y. Gunawardena, Experimental investigation of the behavior of concrete-filled high-strength glass fiber-reinforced polymer tubes under static and cyclic axial compression, Structural Concrete 21 (4) (2020) 1497–1522.

[26] F. Aslani, Y. Gunawardena, A. Dehghani, Behaviour of concrete filled glass fibre-reinforced polymer tubes under static and flexural fatigue loading, Constr. Build. Mater. 212 (2019) 57–76.

[27] J. Zhu, Y. Chen, L.i. Zhang, B. Guo, G. Fan, X. Guan, R. Zhao, Revealing the doping mechanism of barium in sulfoaluminate cement clinker phases, J. Cleaner Prod. 295 (2021) 126405, https://doi.org/10.1016/j.jclepro.2021.126405.

[28] A. Dehghani, F. Aslani, Fatigue performance and design of concrete-filled steel tubular joints: A critical review, J. Constr. Steel Res. 162 (2019) 105749, https://doi.org/10.1016/j.jcsr.2019.105749.

[29] D. Xu, et al., Analytical approach for crack identification of glass fiber reinforced polymer–sea sand concrete composite structures based on strain dissipations. Struct. Health Monitor., **2020**, 1475921720974290 doi: 10.1177/1475921720974290.

[30] J. Liu, C. Wu, G. Wu, X. Wang, A novel differential search algorithm and applications for structure design, Appl. Math. Comput. 268 (2015) 246–269.

[31] Q. Long, C. Wu, X. Wang, A system of nonsmooth equations solver based upon subgradient method, Appl. Math. Comput. 251 (2015) 284–299, https://doi.org/10.1016/j.amc.2014.11.064.

[32] A.T.A. Dantas, M. Batista Leite, K. de Jesus Nagahama, Prediction of compressive strength of concrete containing construction and demolition waste using artificial neural networks, Constr. Build. Mater. 38 (2013) 717–722, https://doi.org/10.1016/j.conbuildmat.2012.09.026.

[33] S. Xu, J. Wang, W. Shou, T. Ngo, A.-M. Sadick, X. Wang, Computer vision techniques in construction: a critical review, Arch. Comput. Methods Eng. 28 (5) (2021) 3383–3397, https://doi.org/10.1007/s11831-020-09504-3.

[34] M. Açikgenç, M. Ulaş, K.E. Alyamaç, Using an artificial neural network to predict mix compositions of steel fiber-reinforced concrete, Arab. J. Sci. Eng. 40 (2) (2015) 407–419.

[35] J. Sun, Y. Wang, X. Yao, Z. Ren, G. Zhang, C. Zhang, X. Chen, W. Ma, X. Wang, Machine-Learning-Aided Prediction of Flexural Strength and ASR Expansion for Waste Glass Cementitious Composite, Appl. Sci. 11 (15) (2021) 6686, https://doi.org/10.3390/app11156686.

[36] J. Sun, Y. Ma, J. Li, J. Zhang, Z. Ren, X. Wang, Machine learning-aided design and prediction of cementitious composites containing graphite and slag powder, J. Build. Eng. 43 (2021) 102544, https://doi.org/10.1016/j.jobe.2021.102544.

[37] Y. Song, X. Wang, G. Wright, D. Thatcher, P. Wu, P. Felix, Traffic volume prediction with segment-based regression kriging and its implementation in assessing the impact of heavy vehicles, IEEE Trans. Intell. Transp. Syst. 20 (1) (2019) 232–243.

[38] V. Singh, N. Gu, X. Wang, A theoretical framework of a BIM-based multi-disciplinary collaboration platform, Autom. Constr. 20 (2) (2011) 134–144.

[39] J. Sun, Y. Huang, F. Aslani, G. Ma, Properties of a double-layer EMW-absorbing structure containing a graded nano-sized absorbent combing extruded and sprayed 3D printing, Constr. Build. Mater. 261 (2020) 120031, https://doi.org/10.1016/j.conbuildmat.2020.120031.

[40] H. Salehi, R. Burgueño, Emerging artificial intelligence methods in structural engineering, Eng. Struct. 171 (2018) 170–189, https://doi.org/10.1016/j.engstruct.2018.05.084.

[41] Y. Sun, G. Li, J. Zhang, J. Sun, J. Xu, Development of an ensemble intelligent model for assessing the strength of cemented paste backfill, Adv. Civil Eng. 2020 (2020) 1–6, https://doi.org/10.1155/2020/1643529.

[42] Y. Sun, J. Zhang, G. Li, G. Ma, Y. Huang, J. Sun, Y. Wang, B. Nener, Determination of Young's modulus of jet grouted coalcretes using an intelligent model, Eng. Geol. 252 (2019) 43–53.

[43] W. Feng, Y. Wang, J. Sun, Y. Tang, D. Wu, Z. Jiang, J. Wang, X. Wang, Prediction of thermo-mechanical properties of rubber-modified recycled aggregate concrete, Constr. Build. Mater. 318 (2022) 125970, https://doi.org/10.1016/j.conbuildmat.2021.125970.

[44] K. Duan, S.S. Keerthi, A.N. Poo, Evaluation of simple performance measures for tuning SVM hyperparameters, Neurocomputing 51 (2003) 41–59.

[45] Hsu, C.-W., C.-C. Chang, and C.-J. Lin, A practical guide to support vector classification. **2003**.

[46] Y. Yu, C. Zhang, X. Gu, Y. Cui, Expansion prediction of alkali aggregate reactivity-affected concrete structures using a hybrid soft computing method, Neural Comput. Appl. 31 (12) (2019) 8641–8660.

[47] C. Wu, X. Wang, M. Chen, M.J. Kim, Differential received signal strength based RFID positioning for construction equipment tracking, Adv. Eng. Inf. 42 (2019) 100960, https://doi.org/10.1016/j.aei.2019.100960.

[48] F. Aslani, J. Sun, D. Bromley, G. Ma, Fiber-reinforced lightweight self-compacting concrete incorporating scoria aggregates at elevated temperatures, Structural Concrete 20 (3) (2019) 1022–1035.

[49] X. Jiang, S. Li, BAS: beetle antennae search algorithm for optimization problems. *arXiv preprint arXiv:1710.10724*, **2017**.

[50] J. Zhang, Y. Sun, G. Li Y. Wang J. Sun J. Li Machine-learning-assisted shear strength prediction of reinforced concrete beams with and without stirrups Eng. Comput., **2020**, 1-15.

[51] J. Sun, X. Wang, J. Zhang, F. Xiao, Y. Sun, Z. Ren, G. Zhang, S. Liu, Y. Wang, Multi-objective optimisation of a graphite-slag conductive composite applying a BAS-SVR based model, J. Build. Eng. 44 (2021) 103223, https://doi.org/10.1016/j.jobe.2021.103223.

[52] C.-M. Huang, Y.-J. Lee, D.K.J. Lin, S.-Y. Huang, Model selection for support vector machines via uniform design, Comput. Stat. Data Anal. 52 (1) (2007) 335–346.

[53] H. Naseri, Cost Optimization of No-Slump Concrete Using Genetic Algorithm and Particle Swarm Optimization, Int. J. Innovat., Manage. Technol. 10 (1) (2019) 33–37.

[54] J. Han, *Principles and Practice of Ground Improvement*. 2014: Principles and Practice of Ground Improvement.

[55] S. Horpibulsuk, N. Miura, T.S. Nagaraj, Assessment of strength development in cement-admixed high water content clays with Abrams' law as a basis, Geotechnique 53 (4) (2003) 439–444.

[56] C. Chen, G. Zhang, J.G. Zornberg, X. Zheng, Element Nail Pullout Tests for Prediction of Soil Nail Pullout Resistance in Expansive Clays, Geotech. Test. J. 42 (5) (2019) 20170431, https://doi.org/10.1520/GTJ1909-EB10.1520/GTJ20170431.

[57] S.K. Lahiri, K.C. Ghanta, The Support Vector Regression with the parameter tuning assisted by a differential evolution technique: Study of the critical velocity of a slurry flow in a pipeline, Chem. Indust. Chem. Eng. Quart. 14 (3) (2008) 191–203, https://doi.org/10.2298/CICEQ0803191L.

[58] S. Boyd, L. Vandenberghe (Eds.), Convex Optimization, Cambridge University Press, 2004.

[59] Wang, J. and H.J.a.p.a. Chen, BSAS: Beetle swarm antennae search algorithm for optimization problems. **2018**.

[60] M. Klammer, J.N. Dybowski, D. Hoffmann, C. Schaab, A.R. Dalby, Pareto Optimization Identifies Diverse Set of Phosphorylation Signatures Predicting Response to Treatment with Dasatinib, PLoS ONE 10 (6) (2015) e0128542, https://doi.org/10.1371/journal.pone.0128542.

[61] K. Yoon, C.-L. Hwang, *Multiple attribute decision making: an introduction*. 1995: Sage publications.

[62] P. Cortez, M.J. Embrechts, Using sensitivity analysis and visualization techniques to open black box data mining models, Inf. Sci. 225 (2013) 1–17, https://doi.org/10.1016/j.ins.2012.10.039.

[63] L. Wang, J. Yuan, C. Wu, X. Wang, Practical algorithm for stochastic optimal control problem about microbial fermentation in batch culture, Optimiz. Lett. 13 (3) (2019) 527–541.

[64] H.J.J.o.M. Åhnberg, Strength of Stabilised Soil - A Laboratory Study on Clays and Organic Soils Stabilised with different Types of Binder. 87 (1), 2006 35-40.

[65] C. Zhang, Control Force Characteristics of Different Control Strategies for the Wind-Excited 76-Story Benchmark Building Structure, Adv. Struct. Eng. 17 (4) (2014) 543–559, https://doi.org/10.1260/1369-4332.17.4.543.

[66] P. Feng, H. Chang, X. Liu, S. Ye, X. Shu, Q. Ran, The significance of dispersion of nano-SiO2 on early age hydration of cement pastes, Mater. Des. 186 (2020) 108320, https://doi.org/10.1016/j.matdes.2019.108320.

[67] L.i. Sun, Z. Yang, Q. Jin, W. Yan, Effect of Axial Compression Ratio on Seismic Behavior of GFRP Reinforced Concrete Columns, Int. J. Struct. Stab. Dyn. 20 (06) (2020) 2040004, https://doi.org/10.1142/S0219455420400040.

[68] D. Wang, Y. Ju, H. Shen, L. Xu, Mechanical properties of high performance concrete reinforced with basalt fiber and polypropylene fiber, Constr. Build. Mater. 197 (2019) 464–473, https://doi.org/10.1016/j.conbuildmat.2018.11.181.

[69] R. Zhao, L.i. Zhang, B. Guo, Y. Chen, G. Fan, Z. Jin, X. Guan, J. Zhu, Unveiling substitution preference of chromium ions in sulphoaluminate cement clinker phases, Compos. B Eng. 222 (2021) 109092.

[70] C. Chen, G. Zhang, J.G. Zornberg, A.M. Morsy, J. Huang, Interface bond behavior of tensioned glass fiber-reinforced polymer (GFRP) tendons embedded in cemented soils, Constr. Build. Mater. 263 (2020) 120132, https://doi.org/10.1016/j.conbuildmat.2020.120132.

[71] L. Blanco Martín, M. Tijani, F. Hadj-Hassen, A new analytical solution to the mechanical behaviour of fully grouted rockbolts subjected to pull-out tests, Constr. Build. Mater. 25 (2) (2011) 749–755.

[72] S. Ma, J. Nemcik, N. Aziz, An analytical model of fully grouted rock bolts subjected to tensile load, Constr. Build. Mater. 49 (2013) 519–526.